

4

**Tectonic evolution of the Salton Sea
inferred from seismic reflection data**

Tectonic evolution of the Salton Sea inferred from seismic reflection data

D. S. Brothers^{1*}, N. W. Driscoll¹, G. M. Kent¹, A. J. Harding¹, J. M. Babcock¹ and R. L. Baskin²

Oblique extension across strike-slip faults causes subsidence and leads to the formation of pull-apart basins such as the Salton Sea in southern California. The formation of these basins has generally been studied using laboratory experiments or numerical models^{1–4}. Here we combine seismic reflection data and geological observations from the Salton Sea to understand the evolution of this nascent pull-apart basin. Our data reveal the presence of a northeast-trending hinge zone that separates the sea into northern and southern sub-basins. Differential subsidence (>10 mm yr⁻¹) in the southern sub-basin suggests the existence of northwest-dipping basin-bounding faults near the southern shoreline, which may control the spatial distribution of young volcanism. Rotated and truncated strata north of the hinge zone suggest that the onset of extension associated with this pull-apart basin began after ~0.5 million years ago. We suggest that slip is partitioned spatially and temporally into vertical and horizontal domains in the Salton Sea. In contrast to previous models based on historical seismicity patterns⁵, the rapid subsidence and fault architecture that we document in the southern part of the sea are consistent with experimental models for pull-apart basins¹.

Our current understanding of the kinematics and evolution of pull-apart basins is based largely on laboratory^{1–3} and numerical models⁴, with few well-dated field studies examining the regional deformation patterns within active pull-apart basins. The San Andreas fault–Imperial fault (SAF–IF) transtensional step-over is an ideal locale to study the relationship between horizontal and vertical deformation in an active pull-apart basin using regional-scale, high-resolution geophysical methods⁶. This step-over delineates the northward transition from the obliquely divergent Gulf of California margin to transpressional deformation of the San Andreas fault system. Early crustal models suggested that much of the southern Salton Trough is underlain and intruded by young, mafic material^{7,8}. Geophysical and thermal anomalies along with volcanism near the southern Salton Sea were attributed to a buried spreading centre between the SAF and IF (refs 7, 8). Later studies examined seismicity patterns and the kinematics of moderate-to-strong earthquakes in the region^{9–11}. The complex ladder-like seismicity patterns of the Brawley Seismic Zone (BSZ; Fig. 1) and faulting to the west of the Salton Sea led to models of distributed dextral shear and block rotation between the SAF and San Jacinto fault (SJF; ref. 5). At present, a consistent model for basin evolution is needed that accounts for the high subsidence rates observed in this study, the seismicity patterns¹¹, the prominent northeast-trending thermal anomaly¹² and string of Quaternary volcanic buttes¹³ (Fig. 1).

Between 2006 and 2008, we acquired over 1,000 line-km of high-resolution chirp seismic reflection data in the Salton Sea (Fig. 1). Sediments deposited during the late Holocene in Lake

Cahuilla¹⁴ (herein referenced as the Cahuilla Formation, CFm) blanket the basin and are defined by parasequence sets that have been radiocarbon dated at onshore sites¹⁵. The sedimentary packages record shoreline fluctuations of Lake Cahuilla, enabling us to correlate high- and low-amplitude reflectors offshore with dated sequences onshore. In the Salton Sea, the CFm records deformation for at least 12 transgression–regression cycles (~2–3 kyr BP). Numerous faults are identified in the CFm by vertically offset reflectors and occasionally by seafloor scarps. Potential correlations between onshore and offshore structures include the Extra fault zone^{9,16} (EFZ) and possibly the Elmore Ranch fault¹⁷ (ERF); both show sinistral slip west of the Salton Sea. Although historic seismicity is scarce along the newly mapped faults^{9,11}, palaeoearthquakes have produced over 1 m of vertical offset per event (see Supplementary Fig. S4). The average strike of faults in the southern sea (N15° E; Fig. 1c) is more northerly than the cross-faults west of the Salton Sea and the short (<5 km) ~N40° E trending seismicity lineaments in the BSZ.

The northeast-striking EFZ, expressed in the CFm as a series of down-to-the-southeast growth folds and faults, seems to be a structural hinge zone that separates the sea into northern and southern basins (Fig. 2). In the northern basin, an angular unconformity separates parallel, concordant reflectors of the CFm from underlying folded and faulted reflectors that we interpret as the Pleistocene Brawley Formation^{16,18} (BFm) mapped west of the sea and at Durmid Hill (DH) (Fig. 1). BFm strata show a progressive increase in dip and fold frequency southward approaching the EFZ, then drop below the limits of acoustic penetration south of the EFZ. The fold geometry provides evidence for broad ~N/S-directed compression and uplift that was subsequently truncated, leaving a nearly flat unconformity surface. The trend of the compression seems to align with subtle topography associated with the San Felipe Anticline west of the sea¹⁶ (Fig. 1). Nevertheless, we do not observe stratigraphic evidence within the CFm for differential subsidence or uplift north of the EFZ.

The EFZ marks the northern limit of active extension. South of the EFZ, CFm beds show marked divergence and evidence for syntectonic sedimentation. Average subsidence measured over the AD 830 time-horizon just south of the hinge zone is between 9 and 12 mm yr⁻¹ (Fig. 2; Supplementary Fig. S3). The CFm beds continue to diverge to the southeast beyond our data coverage, suggesting that the above estimate is a minimum. Stratal divergence indicates that subsidence is equal to or slightly higher than sedimentation, where the average sedimentation rate in the southern basin has been nearly 19 mm yr⁻¹ since ~AD 1360. The projected location of maximum subsidence is near the southern shoreline, approximately coincident with the locus of Quaternary volcanism and a northeast-trending band of very high heat flow. Farther south, the rapidly subsiding Mesquite Basin bounds the

¹ Scripps Institution of Oceanography, University of California, San Diego, 9500, Gilman Drive, La Jolla, California 92093, USA, ² United States Geological Survey, 2329 West Orton Circle, West Valley City, Utah 84119, USA. *e-mail: dbrother@ucsd.edu.

Tectonic evolution of the Salton Sea inferred from seismic reflection data

D. S. Brothers^{1*}, N. W. Driscoll¹, G. M. Kent¹, A. J. Harding¹, J. M. Babcock¹ and R. L. Baskin²

Oblique extension across strike-slip faults causes subsidence and leads to the formation of pull-apart basins such as the Salton Sea in southern California. The formation of these basins has generally been studied using laboratory experiments or numerical models^{1–4}. Here we combine seismic reflection data and geological observations from the Salton Sea to understand the evolution of this nascent pull-apart basin. Our data reveal the presence of a northeast-trending hinge zone that separates the sea into northern and southern sub-basins. Differential subsidence ($>10\text{ mm yr}^{-1}$) in the southern sub-basin suggests the existence of northwest-dipping basin-bounding faults near the southern shoreline, which may control the spatial distribution of young volcanism. Rotated and truncated strata north of the hinge zone suggest that the onset of extension associated with this pull-apart basin began after ~ 0.5 million years ago. We suggest that slip is partitioned spatially and temporally into vertical and horizontal domains in the Salton Sea. In contrast to previous models based on historical seismicity patterns⁵, the rapid subsidence and fault architecture that we document in the southern part of the sea are consistent with experimental models for pull-apart basins¹.

Our current understanding of the kinematics and evolution of pull-apart basins is based largely on laboratory^{1–3} and numerical models⁴, with few well-dated field studies examining the regional deformation patterns within active pull-apart basins. The San Andreas fault–Imperial fault (SAF–IF) transtensional step-over is an ideal locale to study the relationship between horizontal and vertical deformation in an active pull-apart basin using regional-scale, high-resolution geophysical methods⁶. This step-over delineates the northward transition from the obliquely divergent Gulf of California margin to transpressional deformation of the San Andreas fault system. Early crustal models suggested that much of the southern Salton Trough is underlain and intruded by young, mafic material^{7,8}. Geophysical and thermal anomalies along with volcanism near the southern Salton Sea were attributed to a buried spreading centre between the SAF and IF (refs 7, 8). Later studies examined seismicity patterns and the kinematics of moderate-to-strong earthquakes in the region^{9–11}. The complex ladder-like seismicity patterns of the Brawley Seismic Zone (BSZ; Fig. 1) and faulting to the west of the Salton Sea led to models of distributed dextral shear and block rotation between the SAF and San Jacinto fault (SJF; ref. 5). At present, a consistent model for basin evolution is needed that accounts for the high subsidence rates observed in this study, the seismicity patterns¹¹, the prominent northeast-trending thermal anomaly¹² and string of Quaternary volcanic buttes¹³ (Fig. 1).

Between 2006 and 2008, we acquired over 1,000 line-km of high-resolution chirp seismic reflection data in the Salton Sea (Fig. 1). Sediments deposited during the late Holocene in Lake

Cahuilla¹⁴ (herein referenced as the Cahuilla Formation, CFm) blanket the basin and are defined by parasequence sets that have been radiocarbon dated at onshore sites¹⁵. The sedimentary packages record shoreline fluctuations of Lake Cahuilla, enabling us to correlate high- and low-amplitude reflectors offshore with dated sequences onshore. In the Salton Sea, the CFm records deformation for at least 12 transgression–regression cycles ($\sim 2\text{--}3\text{ kyr BP}$). Numerous faults are identified in the CFm by vertically offset reflectors and occasionally by seafloor scarps. Potential correlations between onshore and offshore structures include the Extra fault zone^{9,16} (EFZ) and possibly the Elmore Ranch fault¹⁷ (ERF); both show sinistral slip west of the Salton Sea. Although historic seismicity is scarce along the newly mapped faults^{9,11}, palaeoearthquakes have produced over 1 m of vertical offset per event (see Supplementary Fig. S4). The average strike of faults in the southern sea ($N15^\circ E$; Fig. 1c) is more northerly than the cross-faults west of the Salton Sea and the short ($<5\text{ km}$) $\sim N40^\circ E$ trending seismicity lineaments in the BSZ.

The northeast-striking EFZ, expressed in the CFm as a series of down-to-the-southeast growth folds and faults, seems to be a structural hinge zone that separates the sea into northern and southern basins (Fig. 2). In the northern basin, an angular unconformity separates parallel, concordant reflectors of the CFm from underlying folded and faulted reflectors that we interpret as the Pleistocene Brawley Formation^{16,18} (BFm) mapped west of the sea and at Durmid Hill (DH) (Fig. 1). BFm strata show a progressive increase in dip and fold frequency southward approaching the EFZ, then drop below the limits of acoustic penetration south of the EFZ. The fold geometry provides evidence for broad $\sim N/S$ -directed compression and uplift that was subsequently truncated, leaving a nearly flat unconformity surface. The trend of the compression seems to align with subtle topography associated with the San Felipe Anticline west of the sea¹⁶ (Fig. 1). Nevertheless, we do not observe stratigraphic evidence within the CFm for differential subsidence or uplift north of the EFZ.

The EFZ marks the northern limit of active extension. South of the EFZ, CFm beds show marked divergence and evidence for syntectonic sedimentation. Average subsidence measured over the AD 830 time-horizon just south of the hinge zone is between 9 and 12 mm yr^{-1} (Fig. 2; Supplementary Fig. S3). The CFm beds continue to diverge to the southeast beyond our data coverage, suggesting that the above estimate is a minimum. Stratal divergence indicates that subsidence is equal to or slightly higher than sedimentation, where the average sedimentation rate in the southern basin has been nearly 19 mm yr^{-1} since $\sim AD 1360$. The projected location of maximum subsidence is near the southern shoreline, approximately coincident with the locus of Quaternary volcanism and a northeast-trending band of very high heat flow. Farther south, the rapidly subsiding Mesquite Basin bounds the

¹ Scripps Institution of Oceanography, University of California, San Diego, 9500, Gilman Drive, La Jolla, California 92093, USA, ² United States Geological Survey, 2329 West Orton Circle, West Valley City, Utah 84119, USA. *e-mail: dbrother@ucsd.edu.

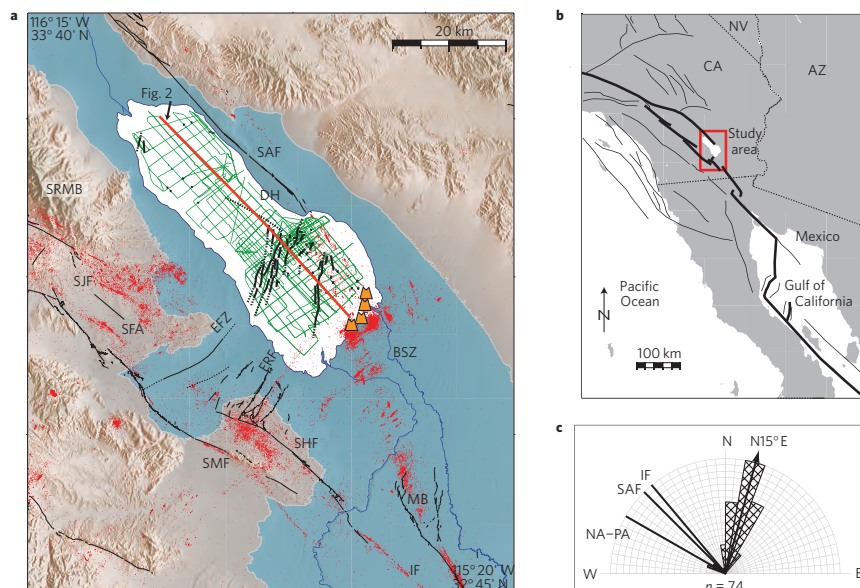


Figure 1 | Map of the Salton Sea region. **a**, Green lines represent seismic reflection profiles (the red line is the location for Fig. 2). Lake Cahuilla is shaded blue. Black lines denote Holocene faults, red dots are relocated earthquakes¹¹ and orange triangles are volcanic buttes. Abbreviations: SRMB, Santa Rosa mountain block; SJF, San Jacinto fault; EFZ, Extra fault zone; ERF, Elmore Ranch fault; BSZ, Brawley seismic zone; SAF, San Andreas fault; SHF, Superstition Hills fault; SMF, Superstition Mountain fault; IF, Imperial fault; DH, Durmid Hill; SFA, San Felipe anticline; MB, Mesquite basin. **b**, Regional map of study area. Abbreviations: CA, California; AZ, Arizona; NV, Nevada. **c**, Rose diagram of fault strikes. The average strike for faults in the sea is N15° E (see the Methods section). Other trends are the SAF, IF and North America–Pacific (NA–PA) plate motion vector at this latitude³⁰.

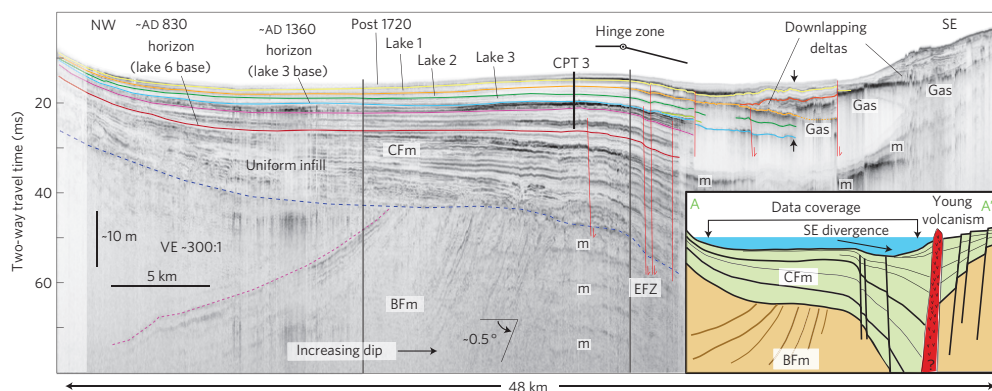


Figure 2 | Salton Sea long-axis seismic reflection profile. A truncation surface (dashed blue line) separates the Holocene CFm from the underlying Pleistocene BFm. Coloured horizons represent time horizons in the CFm; red lines denote faults; black arrows mark the location at which sedimentation rate was estimated; multiple reflections (acoustic artefacts) are identified by 'm'. The black pipe labelled CPT-3 represents cone penetration test data (see Supplementary Fig. S1). Inset, Interpretive cross-section. North of the EFZ, reflectors in the CFm are concordant and record little deformation. Reflectors in the BFm show evidence for ~N/S-oriented compression. South of the EFZ, layers diverge and thicken. We infer that maximum subsidence occurs near the southern shoreline and that extensional faults may provide fluid migration pathways for young volcanism.

northern terminus of the IF and seems to define a separate pull-apart basin^{19,20} within the larger SAF–IF step-over (Fig. 1).

If we assume that subsidence is equal to or slightly greater than sedimentation ($\sim 20 \text{ mm yr}^{-1}$) and that an inferred boundary fault (assumed strike/dip = N30° E/60° N) accommodates most of the subsidence, then horizontal extension is calculated at 11.5 mm yr^{-1} in the direction N60° W (orthogonal to the boundary

fault). Projected onto an azimuth parallel to the SAF, this yields $\sim 11.2 \text{ mm yr}^{-1}$ of dextral slip. Although long-term slip-rate estimates for the southern SAF are few and somewhat controversial, offset alluvial fans north of the Salton Sea provide a rate between 9 and 15 mm yr^{-1} over the past 45–50 kyr (ref. 21), whereas the short-term geodetic rate is $23.3 \pm 0.5 \text{ mm yr}^{-1}$ (ref. 22). Should the long-term rate be more representative, 75–100% of the horizontal

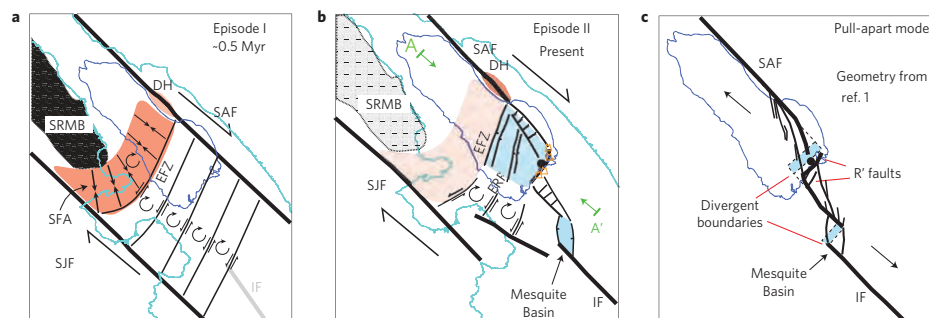


Figure 3 | Map-view models for the tectonic evolution of the Salton Sea. Bold faults represent the primary tectonic structures; orange triangles are volcanic buttes¹³. Blue shades are extensional domains; light-red zones are inactive compression; dark-red zones are active compression; the blue line is the Lake Cahuilla high-shoreline. Green arrows define the extent of the cross-sectional view in Fig. 2 (inset). **a**, Block rotation between the SAF and the SJF and compression north of the EFZ at ~ 0.5 Myr. **b**, Development of SAF–IF step-over and present-day configuration. **c**, Physical model of a pull-apart basin with mechanical layering¹ (superimposed on the Salton Sea). Extension is focused along R' faults above the divergent boundary, forming an asymmetric basin. The Mesquite Basin represents a separate pull-apart basin within the SAF–IF step-over.

slip transferred from the SAF into the Salton Sea is accommodated by extension and subsidence, leaving less than 4 mm yr^{-1} for intrabasin strike-slip faulting and/or rotation. If we assume that the geodetic rate is more representative, then only $\sim 50\%$ of SAF slip is converted to extension in the sea. The ratio of horizontal slip to vertical subsidence constrains the relative importance of slip partitioning in this evolving pull-apart basin.

The EFZ and projected ERF show consistent down-to-the-east vertical displacement beneath the Salton Sea; these observations call into question the relationship between the onshore and offshore structures. If they represent the same fault segments, their trends and kinematics change as they extend into the SAF–IF step-over. Studies examining cross-faults west of the Salton Sea and seismicity in the BSZ (refs 5, 9, 23) would not have observed the large component of extension and subsidence occurring within the sea. We contend that the $\sim N15^\circ E$ striking faults and inferred boundary fault in the southern sea produce relatively infrequent, but large, earthquakes (magnitude $M > 6$) that accommodate extension and subsidence, whereas the smaller events ($M < 5$) and microseismicity that define the BSZ are due to fracturing and block rotation within a narrow (< 5 -km-wide), dextral shear zone. In essence, the southern sea seems to be slip-partitioned into two separate tectonic domains. Contrary to previous models⁵, we argue that block rotation alone cannot generate the observed rapid subsidence, the northeast-trending collection of volcanic buttes, and the thermal and geophysical anomalies along the southern shoreline^{8,12,13}. These observations are more consistent with a large component of extension. Understanding the kinematics of the SAF–IF step-over may depend on the observation timescale. Extension and subsidence dominate over hundreds of years through ground-rupturing ($M > 6$) normal-oblique earthquakes, where the BSZ releases strain over decadal scales through numerous small-to-moderate earthquakes^{10,11} and aseismic processes²⁴. Sinistral cross-faults west of the Salton Sea have low slip-rates ($\sim 1 \text{ mm yr}^{-1}$; ref. 23) and seem to be secondary structures responding to rotation within the broader SAF–SJF strain field⁵.

We propose a conceptual two-stage model for tectonic evolution for the Salton Sea. Though poorly understood, Episode I is characterized by the transpression observed north of the EFZ. Here, the EFZ may have started as a transpressional boundary between the SAF and SJF, before the development of the SAF–IF step-over (Fig. 3a). As the SJF formed, clockwise rotating blocks bounded by northeast-striking sinistral faults accommodated strain distributed between the SAF and SJF (ref. 5). One scenario is that block

boundaries were not defined by simple, linear faults, but contained geometric complexities that produced vertical deformation. As rotation proceeded, block margins west of the Salton Sea are expected to have translated northward, impinging onto the Santa Rosa Mountains and resulting in $\sim N/S$ -oriented compression recorded in the sediments beneath the Salton Sea.

Episode II marks the onset of extension in the Salton Sea and development of the present-day transtensional regime (Fig. 3b). As the SAF–IF step-over formed, compression waned and some of the cross-faults that formed during Episode I began to accommodate normal slip. The differential subsidence and normal slip observed across northeast-striking faults began with the formation or northward propagation of the IF. Fault and subsidence patterns support bulk surface displacement being roughly parallel to plate motion. As extension progressed, subsidence became focused in the southern sea along an inferred north-dipping basin-bounding fault zone that we believe resembles R' faults in physical models of pull-apart basins¹ (Fig. 3b,c). Maximum subsidence occurs in the hanging wall of R' faults directly above the divergent boundary, producing hinge zone roll-over and stratal divergence¹. These boundary faults may enhance decompression melting and provide migration pathways for volcanic and hydrothermal fluids (Fig. 2 (inset)). Similarities between observed structure and physical models suggest that the Salton Sea is in an early to mid-stage of development, but the overall SAF–IF step-over is relatively immature^{1,2}. Short sinistral faults in the BSZ (ref. 5) may reflect internal deformation and rotation within strike-slip shear zones, as predicted in physical models¹ (Fig. 3b,c). Through time, deformation is expected to broaden where the Salton Sea and Mesquite Basin coalesce to form a composite pull-apart basin²⁵.

Although the absolute age of each deformational episode remains poorly constrained, this study provides relative ages for the deformation and an upper bound on the age of the SAF–IF step-over. In our model, the compression of the BFM beneath the angular unconformity is contemporaneous with, or postdates, the onset of deformation along the southern SJF zone (1.1–1.3 Myr; ref. 26). Subsequently, a structural reorganization that established N/S-directed compression to the west of the Salton Sea occurred at ~ 0.5 – 0.6 Myr (refs 16, 27), approximately the same time that deposition of BFM ended¹⁶. Assuming that the structural reorganization coincides with Episode I, we argue that the compression in the BFM north of hinge occurred sometime after ~ 0.5 Myr. Compression was then replaced by extension south of the EFZ, thus providing a maximum age for the formation

of the SAF–IF step-over at ~ 0.5 Myr. Erosion of onshore BFM strata may present a significant lacuna, therefore a late-Pleistocene¹⁹ (~ 0.1 Myr) age for the SAF–IF is possible.

In summary, our observations provide important constraints on the growth of an active pull-apart basin and the evolution of the southern SAF system. On the basis of our interpretive model we conclude the following. (1) Differential subsidence south of the EFZ has produced an asymmetric basin with strata thickening southward into a basin-bounding fault system. (2) Transtension beneath the Salton Sea is partitioned into distinct extensional and strike-slip domains. Extensional faults are at a high angle to the SAF, rupture during larger, less frequent earthquakes and should be considered seismically hazardous. The BSZ accommodates dextral shear transferred into the basin through internal deformation (for example secondary faulting and/or rotation). (3) The Salton Sea basin seems similar to young pull-apart basins in physical models and provides a comparative example on the basis of high-fidelity records of deformation. Our proposed model is the first to account for the rapid subsidence, elevated heat flow and profuse seismicity in the Salton Sea.

Methods

Seismic reflection data were collected using Scripps Institution of Oceanography's Edgetech 512i sub-bottom profiler, herein referred to as a chirp system. Each shot was digitally recorded and included real-time GPS navigation. Profiles were processed using SIOSEIS then imported into the Kingdom Suite and IVS Fledermaus software packages for interpretation. Vertical resolution between reflectors is ~ 15 – 40 cm, depending on the source pulse and sediment velocity, and vertical penetration is up to ~ 70 m. Time-to-depth conversions assumed a sediment velocity of $1,600 \text{ m s}^{-1}$. Seismic sections were interpreted using considerable vertical exaggeration (as in Fig. 2) to delineate subtle changes in stratal geometry and identify regional scale variation. All faults shown in Fig. 1 offset the CFm and typically dip between 50° and 70° (faults in Fig. 2 seem vertical owing to vertical exaggeration). Fault statistics (Fig. 1c) were not normalized by fault length because many faults extend beyond the data coverage.

The CFm consists of unconsolidated fluvio-lacustrine facies deposited during Colorado River diversions, but before the formation of the Salton Sea (1905). Between 2003 and 2006, United Research Services collected 17 sediment borings and 34 cone penetration tests in the Salton Sea²⁸. These data provide information on the lithostratigraphy that can be correlated with the acoustic properties observed in chirp profiles. High-amplitude horizons correspond to lowered lake levels and the consequent increased silt/sand components detected by cone penetrometer tests²⁸; low-amplitude horizons represent fine-grained high-stand lake deposits. Correlating the onshore¹⁵ and offshore lake sequences enables us to establish a chronostratigraphic framework that is used to constrain the deformation history beneath the sea (see Supplementary Fig. S1). The most recent Lake Cahuilla high-stand occurred around AD 1680–1720 and up to six high-stands have been dated back to \sim AD 800 (refs 15, 29). Dated horizons were correlated spatially between chirp profiles to construct isopach maps and estimate differential subsidence rates.

Received 6 January 2009; accepted 30 June 2009;
published online 26 July 2009

References

- Basile, C. & Brun, J. P. Transtensional faulting patterns ranging from pull-apart basins to transform continental margins: An experimental investigation. *J. Struct. Geol.* **21**, 23–37 (1999).
- Wu, J. E., McClay, K., Whitehouse, P. & Dooley, T. 4D analogue modelling of transtensional pull-apart basins. *Mar. Petrol. Geol.* (in the press).
- McClay, K. & Dooley, T. Analogue models of pull-apart basins. *Geology* **23**, 711–714 (1995).
- Katzman, R., ten Brink, U. S. & Lin, J. A. 3-Dimensional modeling of pull-apart basins—implications for the tectonics of the dead-sea basin. *J. Geophys. Res.* **100**, 6295–6312 (1995).
- Nicholson, C., Seeber, L., Williams, P. & Sykes, L. R. Seismic evidence for conjugate slip and block rotation within the San-Andreas Fault System, Southern California. *Tectonics* **5**, 629–648 (1986).
- Seeber, L. *et al.* Rapid subsidence and sedimentation from oblique slip near a bend on the North Anatolian transform fault in the Marmara Sea, Turkey. *Geology* **34**, 933–936 (2006).
- Elders, W. A., Biehler, S., Rex, R. W., Robinson, P. T. & Meidav, T. Crustal spreading in Southern California. *Science* **178**, 15–24 (1972).
- Fuis, G. S., Mooney, W. D., Healy, J. H., McMechan, G. A. & Lutter, W. J. A seismic refraction survey of the Imperial-Valley Region, California. *J. Geophys. Res.* **89**, 1165–1189 (1984).
- Hudnut, K. *et al.* Surface ruptures on cross-faults in the 24 November 1987 Superstition Hills, California, earthquake sequence. *Bull. Seismol. Soc. Am.* **79**, 282–296 (1989).
- Hardebeck, J. L. & Shearer, P. M. Using S/P amplitude ratios to constrain the focal mechanisms of small earthquakes. *Bull. Seismol. Soc. Am.* **93**, 2434–2444 (2003).
- Lin, G. Q., Shearer, P. M. & Hauksson, E. Applying a three-dimensional velocity model, waveform cross correlation, and cluster analysis to locate southern California seismicity from 1981 to 2005. *J. Geophys. Res.* **112**, B12309 (2007).
- Newmark, R. L., Kasameyer, P. W. & Younker, L. W. Shallow drilling in the Salton-Sea Region—the thermal anomaly. *J. Geophys. Res.* **93**, 13005–13023 (1988).
- Schmitt, A. K. & Vazquez, J. A. Alteration and remelting of nascent oceanic crust during continental rapture: Evidence from zircon geochemistry of rhyolites and xenoliths from the Salton Trough, California. *Earth Planet. Sci. Lett.* **252**, 260–274 (2006).
- Waters, M. R. Late holocene lacustrine chronology and archaeology of ancient Lake Cahuilla, California. *Quat. Res.* **19**, 373–387 (1983).
- Philibosian, B. *Paleoseismology of the San Andreas Fault at Coachella, California*. Master's thesis, Univ. Oregon (2007).
- Kirby, S. M. *et al.* Pleistocene brawley and ocotillo formations: Evidence for initial strike-slip deformation along the San Felipe and San Jacinto fault zones, southern California. *J. Geol.* **115**, 42–62 (2007).
- Hudnut, K. W., Seeber, L. & Pacheco, J. Cross-fault triggering in the November 1987 Superstition Hills earthquake sequence, Southern California. *Geophys. Res. Lett.* **16**, 199–202 (1989).
- Burgmann, R. Transpression along the Southern San-Andreas Fault, Durmid Hill, California. *Tectonics* **10**, 1152–1163 (1991).
- Larsen, S. & Reilinger, R. Age constraints for the present fault configuration in the Imperial Valley, California—evidence for Northwestward propagation of the Gulf of California Rift System. *J. Geophys. Res.* **96**, 10339–10346 (1991).
- Johnson, C. E. & Hadley, D. M. Tectonic implications of the Brawley Earthquake Swarm, Imperial Valley, California, January 1975. *Bull. Seismol. Soc. Am.* **66**, 1133–1144 (1976).
- Behr, W. *et al.* SCEC Annual Meeting, Proceedings and Abstracts Vol. 17, 87 (2007).
- Meade, B. J. & Hager, B. H. Block models of crustal motion in southern California constrained by GPS measurements. *J. Geophys. Res.* **110**, B04402 (2005).
- Hudnut, K. W., Seeber, L. & Rockwell, T. Slip on the Elmore Ranch Fault during the past 330 years and its relation to slip on the Superstition Hills Fault. *Bull. Seismol. Soc. Am.* **79**, 330–341 (1989).
- Lohman, R. B. & McGuire, J. J. Earthquake swarms driven by aseismic creep in the Salton Trough, California. *J. Geophys. Res.* **112**, B04405 (2007).
- Aydin, A. & Nur, A. Evolution of pull apart basins and their scale independence. *Tectonics* **1**, 91–105 (1982).
- Steeley, A. N., Janicke, S. U., Dorsey, R. J. & Axen, G. J. Early Pleistocene initiation of the San Felipe fault zone, SW Salton Trough, during reorganization of the San Andreas fault system. *Geol. Soc. Am. Bull.* **121**, 663–687 (2009).
- Lutz, A. T., Dorsey, R. J., Housen, B. A. & Janicke, S. U. Stratigraphic record of Pleistocene faulting and basin evolution in the Borrego Badlands, San Jacinto fault zone, Southern California. *Geol. Soc. Am. Bull.* **118**, 1377–1397 (2006).
- URS. Preliminary in-sea geotechnical investigation, Salton Sea Restoration Project Report (Riverside and Imperial Counties, 2004).
- Meltzner, A. J., Rockwell, T. K. & Owen, L. A. Recent and long-term behavior of the Brawley Fault Zone, Imperial Valley, California: An escalation in slip rate? *Bull. Seismol. Soc. Am.* **96**, 2304–2328 (2006).
- Kreemer, C., Holt, W. E. & Haines, A. J. An integrated global model of present-day plate motions and plate boundary deformation. *Geophys. J. Int.* **154**, 8–34 (2003).

Acknowledgements

Funding for this work was provided by the California Department of Water Resources, California Department of Fish and Game, UCSD Academic Senate, Scripps Institution of Oceanography, National Science Foundation (grants OCE-0112058 and EAR-0545250) and Southern California Earthquake Center (grant 2008-08127). We would like to thank B. Philibosian, D. Sandwell and D. Kilb for discussions, and V. Langenheim for a review.

Author contributions

D.S.B. planned field surveys, collected, analysed and interpreted the data and wrote the manuscript. N.W.D. and G.M.K. planned field surveys, collected and interpreted the data and provided extensive feedback on the manuscript. A.J.H., J.M.B. and R.L.B. collected data and provided feedback on the manuscript.

Additional information

Supplementary information accompanies this paper on www.nature.com/naturegeoscience. Reprints and permissions information is available online at <http://mpg.nature.com/reprintsandpermissions>. Correspondence and requests for materials should be addressed to D.S.B.

5

Late-Holocene Earthquake and Sedimentary History Beneath the Salton Sea, Southern California

5.1 ABSTRACT

Marine paleoseismic investigations in the Salton Sea uncovered more than 15 vertical displacement events along a series of \sim N15°E oriented faults. Seismic CHIRP profiles imaged more than fourteen Lake Cahuilla (LC) parasequences (2-3 kyr B.P.). Calendar age estimates for the six most recent parasequences (\sim 830 AD - present) are obtained by correlating acoustic stratigraphy in the Salton Sea with onshore sequences that have been radiocarbon dated. Faults to the southwest of Bombay Beach have produced up to 10 events in the last 2-3 kyr. Since \sim 830 AD, vertical slip rates range from 1.1 to 3.4 mm/yr and average recurrence intervals range from 115 years to 460 years. Seafloor scarps and deformed Salton Sea sediments imply recent offset, possibly aseismic creep and/or triggered slip. Evidence for slip inversion suggests fault kinematics has changed over short timescales ($<$ 1000 years). As faults extend farther west their vertical displacement and recurrence intervals appear to decrease, but contain evidence for at least 2 events in the LC section. Faults discovered in the northern sea show evidence

for at least two events in the LC section, but are generally less active. Only 2 of the last 5 events on the southern San Andreas Fault (SAF) were potentially synchronous with events offshore. Based on the relationship between flooding surfaces and fault displacements, it appears that ruptures on three offshore faults occur when the Colorado River floods the basin. Assuming strain is released seismically, faults in the Salton Sea can potentially generate M6-6.8 earthquakes, which could act as a stress modulator on the southern SAF, which may have been the case for the 3rd and 5th ruptures back in time during large flood events.

5.2 INTRODUCTION

5.2.1 Paleoseismology in the Salton Sea

The Salton Sea is a large (~970 km²), shallow lake located in the central Salton Trough of Southern California that covers the southernmost extension of the San Andreas Fault (SAF; Figure 1) and the northernmost transtensional step-over associated with Gulf of California oblique rifting. Brothers et al. (2009) mapped numerous faults and defined the shallow basin architecture. They proposed that rapid subsidence in the southern Salton Sea is due to oblique extension within the San Andreas Fault- Imperial Fault (SAF-IF) step-over, one of few places in the Salton Trough undergoing active lithospheric thinning, and that several faults in the Salton Sea have the potential to produce relatively frequent M>6 earthquakes. In this paper we expand on the results of Brothers et al. (2009) by performing a detailed investigation of paleoseismic deformation along faults in the Salton Sea. Several studies have suggested the southernmost SAF is overdue for a large-magnitude earthquake (Fialko, 2006). Comprehensive hazard assessments require regional studies that account for rupture along secondary faults and their potential to inhibit or promote failure on the SAF. Therefore, understanding the kinematic

relationships and seismic cycling between the SAF and extensional faults beneath the Salton Sea is of utmost importance.

The Salton Sea offers an opportunity to perform marine paleoseismology along a 50 km-long section of the SAF system. Marine paleoseismology has been successfully applied in extensional domains (Brothers et al., 2009b; Bull et al., 2003; Kent et al., 2005; Lamarche et al., 2006; McHugh et al., 2006), but few places offer multi-event records at decadal-scale resolution. There are significant advantages to working in subaqueous over subaerial environments, namely that sedimentation tends to be more continuous in time and space allowing better preservation of deformed sediment horizons and anthropogenic disturbances are generally less underwater. In addition high-resolution geophysics can image deformation at sub-meter resolution, but with much greater spatial coverage than with onshore methods. The goals of this study are to define a detailed late-Holocene depositional framework and deformation history within the submerged portion of the San Andreas-Imperial Fault (SAF-IF) pull-apart basin (Figure 1). We examine coseismic deformation preserved in Lake Cahuilla sediments to obtain constraints on the earthquake history, slip-rates and sedimentation history using detailed analysis of > 1,000 line-km of seismic CHIRP profiles (Figure 2). We also compare paleoearthquake records beneath the Salton Sea with those observed along onshore fault systems, namely the SAF.

5.2.2 The Salton Trough Tectonics

As much as 80% of the contemporary North America-Pacific plate boundary motion is partitioned across the SAF, San Jacinto Fault (SJF) and Imperial Fault (IF) zones (Becker et al., 2005; Meade and Hager, 2005). Slip rates determined for the SAF and SJF vary depending on the study and the timescale. Geodetic studies place their combined rate at between 35 – 40 mm/yr (Fay and Humphreys, 2005; Meade and Hager, 2005), but rates based on geologic data are generally lower, but highly variable (Behr et

al., 2007; Brothers et al., 2009a; Fletcher et al., 2007; Kendrick et al., 2002; Rockwell et al., 1990). At Bombay Beach the SAF takes a transtensional step towards the IF (Figure 1), forming the southern Salton Sea and the Mesquite pull-apart basins (Brothers et al., 2009a). The Salton Sea pull-apart appears asymmetric and is bounded to the north by the Extra Fault hinge-zone and to the south by an inferred boundary fault system near the southern shoreline (Brothers et al., 2009a). Subsidence approaches 20 mm/yr in the southern sea. The SJF splays into several dextral faults west of the Salton Sea, but deformation converges southward onto the Imperial Fault, which takes on the combined SAF and SJF slip-rates at 36 - 40 mm/yr (Lyons et al., 2002; Meade and Hager, 2005). Interseismic creep has been observed throughout the Salton Trough with temporally varying rates between 2 - 20 mm/yr (Lyons and Sandwell, 2003; Lyons et al., 2002; Sieh and Williams, 1990). Fault creep and triggered slip were observed following the Landers, Hector Mine, and Superstition Hills earthquakes (Hudnut et al., 1989b; Lyons and Sandwell, 2003).

The southernmost 200-km of the SAF has not produced a major rupture in ~300+ years despite evidence that the surrounding region continues to accumulate significant strain (Fialko, 2006; Fumal et al., 2002; Philiposian, 2007; Sieh and Williams, 1990). The potential for a M7.0 or greater rupture to nucleate in the Salton Sea and propagate northward along SAF is a major concern (Olsen et al., 2006), but has not been investigated in detail due to an absence of paleoseismic data in the Salton Sea. In addition, few sites along the southern SAF have produced reliable paleoseismic records. At present, Philiposian (2007) presents the most detailed Lake Cahuilla history based on 82 radiocarbon dates and six earthquakes since ~ 800 AD. It is important to determine if faults in the Salton Sea play a role in modulating the earthquake cycle along the SAF.

5.2.3 Lake Cahuilla and the Salton Sea

During the Holocene, the Colorado River would occasionally flow northward into the isolated Salton Basin, forming Lake Cahuilla. When the river resumed flow to the Gulf of California, Lake Cahuilla would begin to evaporate and at times expose the basin to subaerial processes. The sediment record of these flooding-desiccation cycles has been studied along the banks of stream channels and in paleoseismic excavations surrounding the Salton Sea. The most complete record and thoroughly dated Lake Cahuilla section is at a paleoseismic site near Coachella, California (Philibosian, 2007), where seven Lake Cahuilla flooding-desiccation cycles were identified, six of which were precisely dated with radiocarbon analysis. The Coachella site is at 9 m elevation and records Colorado River diversions that completely filled the basin to an elevation of ~13 m, the height of the delta apex south of the international border (Figure 1). In general, the late-Holocene depositional environment cycled through periods of rapid flooding during Colorado River diversions, followed by lower energy lacustrine conditions, then shoreline regression, desiccation and subaerial exposure. Philibosian (2007) characterized parasequences by fine grained, deep water lacustrine facies deposited during Lake Cahuilla high-stands separated by sand and gravel rich fluvial beds associated with low-stand intervals and subaerial exposure. Prior to the present study, the only detailed information on the stratigraphy beneath the Salton Sea was based on bore holes and cone penetration test data (URS, 2004).

During spring runoff in 1905, canal construction weakened the Colorado River's natural levees allowing it to breach its banks and flow northward for 18 months, filling the depression that is now the Salton Sea. The present shoreline has been maintained at ~69 m below sea level by agricultural runoff in the Imperial and Coachella Valleys. Several factors combine to make the Salton Sea an ideal location to use marine geophysical methods to study regional depositional processes and tectonic deformation. First, the

repeated flooding and desiccation cycles associated with Lake Cahuilla formed distinctive marker beds that can be correlated regionally. Second, onshore paleoseismic studies (Meltzner et al., 2006; Philibosian, 2007) have constrained the age of Lake Cahuilla sediments over the last ~6 flooding-desiccation cycles, providing a chronostratigraphic framework that can be extended offshore. Last, sedimentation rates in the sea are high, providing optimal conditions to preserve paleoearthquake evidence over multiple earthquake cycles.

One of the primary goals of this study is to use a chronostratigraphic model to quantify the timing and magnitude of tectonic deformation. In places, sediment accumulation averaged over the last ~1200 years is nearly 2 cm/yr, therefore the ~ 12 cm resolution of the 1-15 kHz CHIRP pulse has the potential to provide decadal-scale resolution during this interval. More than 20 fault segments were mapped beneath the Salton Sea (Figure 2). Some faults show sharp seafloor offset and/or stratigraphic growth down-section, while others are more subtly expressed as growth folds. In general, slip rates on individual faults are an order of magnitude less than sedimentation rates, allowing rapid burial and preservation of coseismic offset. To date, most paleoseismic work on faults is restricted to regions of deposition at a limited number of elevations. By systematically mapping the Salton Sea, we can assess the earthquake and sediment history at multiple elevations and across several fault systems and as such it provides an excellent approach to complement onshore paleoseismic excavations.

5.3 METHODS

Detailed geophysical surveys were conducted in the Salton Sea between 2006 and 2009 (Figure 2). Sub-bottom CHIRP profiles and sidescan sonar imagery were collected using Scripps Institution of Oceanography's Edgetech subscan systems aboard two vessels: a privately owned 50' pontoon vessel and the 23' R/V Stephens (operated by

the USGS). Ancillary swath bathymetry surveys employed a Kongsberg 3002 multibeam system aboard the R/V Stephens. This study is focused on the results from > 1,000 line-km sub-bottom data. All data were digitally recorded in JSF format and included real-time GPS navigation with each shot, providing absolute location accuracy to within 5 m. JSF files were converted to standard SEG-Y format and subsequently processed using *SIOSEIS*, then imported into the *Kingdom Suite* and *Fledermaus* software packages for interpretation. Sidescan data were processed using *xsonar* (Danforth, 1997). Sub-bottom surveys employed different CHIRP pulses depending on sub-bottom conditions. The 0.7 – 3.0 kHz, 50 ms pulse provided greatest penetration (up to 60 m) while the 1.0 – 15.0 kHz, 30 ms pulse produced the highest vertical resolution (~15 cm).

Between 2003 and 2006, United Research Services Corporation (URS Corp.) collected 17 offshore borings and 34 cone penetration tests (CPT) from a self-propelled jack-up barge (URS, 2004). CPTs are primarily used for near-surface stratigraphic profiling. Soundings in the Salton Sea recorded measurements of cone bearing, sleeve friction, and dynamic pore water pressure at 2.5-cm intervals during penetration, thus providing a nearly continuous stratigraphic log in the upper ~20 m. Variations in these measurements can be used to infer changes in sediment type and/or grain size variations with depth (Robertson, 1990). Additionally, Schroeder et al. (2002) generated chemical profiles from a 0.5 m gravity core to identify the pre-Salton Sea sediment horizon and constrain the post-1905 sedimentation rates. Combined, these studies provide information on the lithostratigraphy that can be correlated with the acoustic properties observed in CHIRP profiles. We built a chronostratigraphic framework based on the correlation between radiocarbon-dated parasequences from Philibosian (2007) with offshore seismic stratigraphy. In so doing, resulting offshore model is biased towards the stratigraphic ages defined by Philibosian (2007). Vertically offset horizons and/or hanging wall growth strata were used as paleoearthquake evidence. Lastly, horizons were correlated in three

dimensions and isopach maps were constructed to understand the differential subsidence patterns and rates.

All depth measurements from seismic sections assumed a p-wave velocity of 1600 m/s to avoid overestimates. Several material index properties, including water content and void ratio were measured from bore samples, but these measurements were too sparsely distributed and did not show a consistent trend needed to correct depth measurements for compaction. Clay layers, particularly near the seafloor show water content between 50-80%. Deeper sediments show lower water content and void ratios, suggesting that significant compaction may have occurred. Because hanging wall strata along faults are several meters deeper than the correlative footwall strata, uncorrected compaction in the hanging wall results in underestimates for fault throw and slip-rate estimates. Due to the sparse sampling, we opted to avoid adding further assumptions into the depth measurements and did not apply a decompaction correction; therefore all depth measurements should be taken as underestimates. Nevertheless, CPT profiles superimposed on seismic sections (converted to depth sections assuming 1600 m/s velocity) provide good correlation between amplitude boundaries and lithologic boundaries, suggesting the assumed p-wave velocity and resulting depth measurements are reasonably accurate.

5.4 RESULTS

5.4.1 Sedimentary and stratigraphic framework

Type sections north and south of the hinge zone were used to identify parasequence sets and establish a basin-wide chronostratigraphy (Figures 3, 4). A CHIRP profile co-registered with an alignment of CPT soundings (Figures 3) was used as our initial type-section. CPT data confirmed the relationship between grain size and acoustic amplitude boundaries: high-amplitude layers correlate with increased silt/

sand components deposited during low-stand or flooding events and the low-amplitude horizons represent fine-grained clays deposited during high-stand episodes. At least 14 parasequences are identified based on acoustic character correlated with CPT soundings and the first six are correlated with onshore stratigraphy at the Coachella site (Table 1). Throughout the basin, high-stand deposits tend to mimic underlying topography, but also show slight thickening in topographic lows. Low-stand deposits, however, record different processes to the north and south of the tectonic hinge zone (Brothers et al., 2009). North of the hinge, low-stand deposits tend to downlap onto the underlying strata, thicken shoreward and appear to be sourced from alluvial fans and local ephemeral streams (Figure 4 inset; Figure 5). Nearshore CHIRP profiles in the northern basin reveal distinct alternations between lacustrine facies and lenticular alluvial deposits. Ephemeral streams and washes drain the San Felipe Hills and Santa Rosa Mountains to the northwest as well as the Mecca Hills and Chocolate Mountains to the northeast. Some of the sand/silt rich facies show irregular erosional contacts with overlying deep-water deposits, particularly moving shoreward (Figure 3 inset). Away from shore, the fine-grained lacustrine layers comprise the majority of the LC section.

Sedimentation south of the hinge-zone is dominated by thick, coarse-grained fan delta facies that were deposited rapidly during Colorado River flooding. These layers tend to onlap the hinge zone and show marked thickening towards the southern shoreline (Figure 6), comprising more than 50% of the LC-section. Fine-grained deposition during high-stands and coarse-grained deposits record the differential subsidence in the southern sea in different ways. Fine-grained deposits, with lower acoustic amplitudes, are generally concordant across fault scarps and seafloor topography, where the coarse grained deposits tend to infill and obscure topographic relief. Near surface gas causes acoustic wipe-out zones (AWZ) throughout much of the southern sea and sub-bottom penetration was limited, particularly along the offshore extension of the SAF. In several

places, vertical AWZs, “pipes”, disrupt stratigraphic horizons and extend to the seafloor. Active venting is observed in the water column and at the lake surface. AWZs appear to be confined to certain stratigraphic horizons and exhibit steps or vertical offset across faults.

Parasequence sets are bounded by flooding surfaces (Van Wagoner and Bertram, 1995). South of the hinge-zone, distinguishing between the low-stand coarse grained facies and the coarse flood deposits that fine upward is difficult. Both have similar acoustic signatures, being high amplitude and infilling lows (Figures 5 and 6). To avoid ambiguity, we define basin-wide LC sequences based solely on amplitude boundaries. High-amplitude sections include both low-stand deposits and deposits emplaced during Colorado River flooding (Figures 3, 5 and 6). In correlating between onshore and offshore stratigraphy, we adopt similar nomenclature as Philibosian (2007), where each lake sequence is numbered and includes a coarsening upward lowstand (“S”) and/or fining upward flood deposit (“F”) followed by a fine-grained high-stand sequence (“L”).

A transparent layer above an irregular high-amplitude reflector defines the youngest episode of lacustrine deposition. Based on borings, CPT soundings and gravity cores (Schroeder et al., 2002; URS, 2004), this layer consists of unconsolidated silt and clay deposited subsequent to the 1905-1907 creation of the Salton Sea. Salton Sea deposits (SS; e.g., Figures 3 and 4) are the most widely mapped of all units because the AWZs usually limits penetration and imaging of underlying layers. North of the hinge zone, parasequence sets display higher consistency in thickness and acoustic character than to the south (Figure 5). Salton Sea deposition (SS) since 1907 is less than ~0.5 cm/yr and pinches out in shallow areas, exposing the top of layer 1S at the seafloor (Figure 3). Sidescan images reveal meandering seafloor channels at the top of 1S. 1S has varied thickness and an irregular upper surface (Figure 3). Fine grained, low amplitude layers 1L, 2L and 3L are separated by relatively thin layers 2S and 3S. 2S and 3S downlap

basinward and also thicken towards local sources onshore (Figure 3). CPT soundings detect 2S and 3S as distinct silt/sand layers along the shoreline, but they are not detected in the deepest portions of the basin (Figures 2 and 3). Evidence for erosional scour in 2S or 3S is not observed. Philibosian (2007) defined 4S as a thick accumulation of fluvial and aeolian deposits that was deposited during prolonged subaerial exposure. Profiles north of the hinge zone show distinct evidence for channelization, such as cut and fill structures during 4S (Figure 3). 6S and 9S also exhibit high amplitude acoustic reflectivity. Although layers 5S, 7S, 8S, 10S, 11S and 12S show an increase in acoustic reflectivity compared to high-stand layers, they are relatively thin. Below layer 9S, horizons become more difficult to correlate throughout the basin. Overall, low-stand episodes form lenticular-shaped lobes of coarse-grained material that thicken towards their respective drainages (Figures 3 and 5) and each parasequence contains essentially the same suite of acoustic character as the parasequences above and below.

SS deposits thicken considerably south of the hinge-zone, especially towards the southern shoreline where modern input from the New and Alamo Rivers is greatest. ~ 2 km north of the Salton Buttes, we observe a downlapping sediment wedge that is more than 4.7 m thick (Figure 5), yielding an average sedimentation rate of ~5 cm/yr since 1907. Layer 1S is thickest in the southern basin where the Colorado River formed a delta during flooding between 1905-1907. South of the hinge, we observe a gradational boundary between all high-stand deposits and the underlying flood facies (top low-stand layers). Layer 2S thickens from less than 0.5 m near the hinge to greater than 5.0 m south of the hinge and contains at least 5 internal layers (Figure 5), that progressively onlap and pinch out on the hinge. 2S does not extend as far north as some of the underlying high-amplitude units (4S, 6S, 9S; Figures 5, 6 and 7). Layer 3S is expressed as a single reflector throughout most of the lake and then thickens slightly south of the hinge zone. Layers 4S, 6S and 9S are thick, high amplitude marker beds

that are easily correlated throughout the sea (Figures 3, 5, 6-8). Overall, moving south from the hinge zone, stratigraphic dip progressively increases down-section (Figure 5) and every coarse grained layer diverges and thickens systematically toward the southern shoreline (Brothers et al., 2009a). Sedimentation appears to be approximately 6-10 mm/yr during high stand and low-stand episodes, but during transgressive flooding and fan delta progradation from the Colorado River, sedimentation at times may exceed 30 cm/yr in the southern sea.

5.4.2 Faults and Earthquake Evidence

We will discuss the faults in the hinge zone from east to west. Other faults south of the hinge zone and north of the hinge zone will be discussed subsequently. For discussion purposes, we geographically grouped the faults into the following (Figure 2): the hinge-zone (“H”), southern (“S”) and northern (“N”) faults. Most faults located in the southern sea have an average trend of N15°E (Brothers et al., 2009a). AWZs limited our ability to image faulting throughout much of the southern sea, including the offshore projection of the SAF (Brothers et al., 2009a) and thus, any determination of fault lengths and scaling relationships would be biased. Irregular seafloor topography and disruption in the modern Salton Sea deposits provide some evidence for faulting in this area, but correlating these observations between profiles is difficult (Figure 2).

The hinge-zone defined by Brothers et al. (2009) is a series of relatively short fault segments (Table 2) that bound the northern extent of active extension and subsidence in the SAF-IF pull-apart basin. Figure 5 illustrates the southward divergence and differential subsidence that is inferred to be bounded to the south by a northwest dipping fault zone (Brothers et al., 2009a). Deformation across the hinge zone is almost exclusively down-to-the-southeast and ranges from subtle fault propagation-folds in the west, to very abrupt vertical offset and seafloor scarps to the east (Figures 7 and 8).

5.4.2.1 Eastern Hinge-Zone

Well-defined vertical offsets are observed on faults H7, H8 and H9 (Figures 6-9). These faults provide the most complete paleoseismic records in the Salton Sea. Stratal thickness variations between the footwall and hanging wall contain information on fault movement and the rates and style of deposition. Detailed correlations between the footwall and hanging wall strata have provided over 25 piercing points from which displacements by individual earthquakes can be measured. The total throw measured over the top of 14L for faults H7, H8 and H9 is 7.1 m, 1.7 m and 4.2 m, respectively (Figures 6-8). Each of these faults offset the top of 1L. 1S onlaps the resulting scarp, suggesting each had an event within the last 300 years (Tables 1 and 2). H7, the most extensively mapped fault in the Salton Sea, shows evidence for displacement since it filled in 1907 (Figures 6 and 7). The average vertical displacements-per-event for the H7 and H8 are 0.7 ± 0.2 m and 0.4 ± 0.2 m; maximum offsets are 1.4 ± 0.2 m, 0.6 ± 0.2 , respectively. The sense of slip on fault H9 was inverted after event *i* (Table 2; Figure 7). For example, the average displacement-per-event for the six most recent events is 0.5 ± 0.3 m and -0.3 ± 0.2 m for the three oldest events. The maximum offset measured on H9 is 1.0 m. Paleoevent chronologies were constructed for events that occurred since the end of 7S deposition (Table 3). Using our best estimates for displacement timing, the following average recurrence intervals were calculated: (H7) 145 – 280 years over the last six events, (H8) 385 – 460 years over the last 3 events, and (H9) 115 -255 years over the last six events. The average vertical slip-rates since ~830 AD on H7, H8 and H9 are at least 3.4, 1.1, and 3.4 mm/yr respectively. Average slip rate estimates appear to have decreased from ~830 to present.

Based on acoustic character and infilling of the sequence on the hangingwall, we examine the timing of offset for the different events. Five coincident events (i.e., *b*, *e*, *h*, *l*, *n*) are observed on H7, H8 and H9. To assess when the fault scarp formed, we flatten

the stratigraphy on specific horizons (Figures 8 and 9). To demonstrate where the offset occurred we flatten on the top of the pre-event stratigraphy (Figure 8) and to determine the style of infill we flatten on a post-event layer (Figure 9). Cumulative offset from earthquakes *a-e* is shown in Figure 7c inset. To assess the offset of event *e*, we have to perform two functions. First, we flatten horizons that show no thickness variability across the hangingwall footwall boundary that are beneath the event horizon (Figure 8a). Based on our correlation with the onshore stratigraphy (Philibosian, 2007) the seafloor age at this time is 1260 AD. Next we flatten the horizon that fills the coseismic accommodation (Figure 8b). Such an approach shows that the event horizon, *e*, occurs in a layer of relatively low acoustic reflectivity immediately above a high-amplitude section (Figure 8, dashed red line).

Following this approach we flattened on horizons for events *b*, *e*, *h*, *l*, and *n* (Figure 9). For event *b*, the infilling stratigraphy exhibits high acoustic amplitude, onlaps the scarp and fills the coseismic accommodation. The (black) dashed line in Figure 9 represents the top of the sequence that fills the accommodation. Note the fault offset is at the top of the high amplitude acoustic package (1S) that represents the pre-event stratigraphy and shows no thickness variability across the fault (Figure 9a). For event *e*, the offset occurs above 4S within 3F within a unit of lower acoustic reflectivity (Figure 9b). Moving back in time, event *h* occurs at the top of 6S/5F. As mentioned above, it is often difficult to identify the boundary between the subaerial component of the previous lake and the initial flooding for the nascent lake (Figure 9c). Another event, *l*, is observed in 9S, where thin high-amplitude layers mantle a unit with low acoustic reflectivity (9L). Finally, the last of the five events observed on all three faults is event *n*, which occurs within 11L, a zone of low reflectivity. Flattening pre-event horizons and post-event infilling horizons yields insight into the style of deposition as well as the lake level when offset occurred (e.g., low-stand, S; flooding, F; high-stand, L).

5.4.3 Western Hinge-Zone

Vertical offset decreases towards the west as faults extend away from the SAF-IF extensional domain (Figures 10, 11 and 12). There also appears to be large differences in the earthquake recurrence interval from west to east. In the western hinge zone, because deformation is expressed as folding rather than distinct vertical offset, timing estimates were not straightforward and varied from line to line. Cumulative throw across 9S (Figure 11) provides comparisons of along-strike changes in vertical motion along the hinge zone.

Deformation distributed across H1-H6 is expressed as monocline folds rather than vertical offset (Figures 10 and 11). With the available data, it is difficult to distinguish between growth caused by multiple earthquakes, attenuation up-section into poorly consolidated material or from gradual infill of accommodation. Figure 12 is an example section that illustrates earthquake-timing estimates for faults H1 – H5. Seafloor offset on faults H3 and H4 is less than 20 cm, but can be correlated between profiles (Figure 11). Small offset and/or folding across the 1907 surface is observed on some faults (e.g., H2). Underlying fold growth is not detected until 3L or 4S, implying that prior to 1907 these faults do not show evidence for slip for several hundred years. The maximum displacement amongst faults H1-H4 measured over 6L-base (~830 AD) is ~1.7 m, yielding a vertical deformation-rate of ~1.5 mm/yr. Each of the faults in the western hinge (H1-H6) have nearly equal cumulative offset across the base of 9S of ~ 1.5 m with maximum displacement of ~2 m. The total subsidence since ~830 AD across faults H1-H5 is ~7.5 m, yielding a subsidence rate of ~6.3 mm/yr. Strata continues to diverge south of fault H5 (Figures 11 and 12). Alluvial fan aggradation in the northern portion of these profiles increases the relief (Figure 12). Areas of highly disturbed sediment, domes and sags in are observed throughout the region (Figure 12).

5.4.4 Southern Faults

A series of faults to the southeast of the hinge-zone (S1-S4) offset stratigraphy in the upper 5 m, but deeper offsets are obscured by AWZs (Figures 7 and 13). Each of these faults exhibit down-to-the-southeast vertical offset. One segment, S2, has a clear seafloor scarp associated with the most recent event (MRE) that measured between 0.1 and 0.3 m in height (Figure 13). The scarp associated with fault S2 is steep with no overlying sediment. Total offset was measured on 15 profiles yielding an average of 0.4 ± 0.1 m. A CPT log near Figure 13 helps constrain the depth of sequence boundaries below the AWZ. Displacement during the penultimate event is observed across the top of layer 1L or bottom of 1S. Fault S1 shows subtle growth folding at the same displacement intervals as on S2. S1, S2 and a few additional un-named faults south of H9 (Figures 2 and 7) appear to have had multiple earthquakes in the post-1L sediments.

5.4.5 Northern Faults

Only a few faults are observed in the Holocene LC section to the north of the hinge zone. Numerous folds and faults, however, are observed in the underlying Brawley Formation (Brothers et al., 2009a). The age of these deformed strata is poorly constrained, but is inferred to be late Pleistocene. Reflections below the unconformity surface can be traced throughout most of the northern basin (Figures 3 and 14). Fault N1 (Figures 3) is expressed as a subtle syncline fold in the LC section but has significant deformation in the underlying Brawley Formation. This fault trends subparallel to the SAF for at least 16 km. Individual event offset and timing are difficult to ascertain, but appears to extend into 6L deposits and possibly younger. Burgman (1991) proposed a SAF parallel fault to explain transpression in Durmid Hill (Figure 1). Two north-trending faults along the northwestern shoreline (Figures 2 and 14) can be traced for only ~2.5 km before being obscured by AWZs. They predominantly deform layers below the LC section. Fold

growth is observed in the LC section then increases dramatically in the underlying units. Based on growth patterns, N2 and N3 had at least 2 events during the last few thousand years (Figure 14). A subtle seafloor scarp on fault N4 near the northeastern shoreline is also observed.

5.4.6 Sediment Thickness and Subsidence

The regional bathymetry of the Salton Sea shows a northern and southern basin separated by a saddle. Isopach maps were constructed to examine the thickness of the various lake sequences (Figure 15c-e). Note the isopach maps are truncated to the south because shallow gas prevented imaging the lake sequences. Nevertheless, the spatial distribution revealed some interesting patterns. For example, the depocenter in all three isopach maps is shifted to the southeast from the present day deepest water depth (Figure 15). The sediment thickness in combination with the onshore stratigraphy were used to calculate the subsidence rates and sediment accumulation in the Salton Sea. Even though the depocenter for the lake sequences are offset from the bathymetry, it is clear the hinge-zone delineates the abrupt thickness increase to the south (Figure 15). Dipping strata appear to extend farther south towards the Salton Buttes and CPT soundings in the southern sea (Figure 16) indicate the stratigraphy continues to deepen to the south beneath the gas. Table 4 summarizes subsidence estimates over horizons 3L, 6L and 8L.

5.5 DISCUSSION

5.5.1 Lake cahuilla stratigraphy

The seismic CHIRP profiles capture the importance of Colorado River sedimentation in filling tectonic accommodation in the southern Salton Sea. The tectonic subsidence identified by Brothers et al. (2009) plays a large role in the deposition patterns observed in the Salton Sea. The regions north and south of the hinge-zone

record different depositional processes due to differential relief and proximity to the Colorado River during lake-filling events. The region north of the hinge is mostly devoid of thick high acoustic amplitude packages inferred to be fan delta deposits (Figure 5). Ephemeral streams that drain local relief supply coarse-grained sediment to the northern basin during episodic storms. As such, the subaerial horizon in the northern part of the lake is a desiccation surface with locally derived fluvial sediment. In contrast in the southern sea, steep relief is far from the Salton Sea, and thus there is no mechanism to transport this coarse grained sediment from the distant relief to the basin (Figure 1). In contrast, the rapidly subsiding southern sea is filled with proximal Colorado River deposits. Most of the sediment deposited by the Colorado River delta onlaps the hinge zone and back steps landward as the shoreline transgresses (Figure 5). Nevertheless, in lacustrine environments during arid episodes or when the Colorado River is not flowing, little sediment is supplied to the basin during lowstands. We surmise that the majority of high amplitude packages that are observed at the base of each lake sequence in the southern Salton Sea are sourced from the Colorado River as flooding commences. Often it is difficult to identify the surface that separates the subaerial portion of the previous lake from the flooding stage of the nascent lake. Where possible we separate the subaerial component from flooding component of the strata, but in some units they are indistinguishable (e.g., 4S/3F and 6S/5F).

Assuming the entire flow of the Colorado River is diverted to the Salton Basin (Van De Kamp, 1973), the amount of time required to fill LC to high-shoreline is approximately 20 years. The transition from fan delta facies to deep-water lacustrine facies beneath the Salton Sea is probably coincident with the filling of the basin. Therefore, the base of each correlative lacustrine unit onshore and offshore is assumed to be equivalent in age. Van de Kamp (1973) estimated that once the Colorado River diverts back to the Gulf of California, Lake Cahuilla evaporates at ~ 1.8 m/yr, causing exposure

beneath the Salton Sea to occur nearly 60 years later than at the high shoreline. Based on these relationships, we established a chronostratigraphic framework for the facies observed beneath the Salton Sea (Table 1). Based on the average sedimentation rate since ~830 AD the older, undated lake sequences are not expected to be older than 3,000 years.

Deposition is highly variable over century-long time scales. South of the hinge, 2S, 4S, 6S, and 9S are distinctive layers where thick, coarse-grained sediments appear to have accumulated very quickly. Based on the acoustic character and stratal geometry, it appears that 4S, 6S and 9S contain sediment that was deposited during flooding into a dry basin. The modern delta sedimentation rates and the estimated time required to fill Lake Cahuilla suggests that these coarse grained units accumulated in 10-20 years (Pratson et al., 2008). Intervals 2S, 3S, 5S, 7S, 10S, 11S, 12S and 13S are relatively thin, which suggests the Colorado River sediment was dispersed into a shallow lake. Migration of the Colorado River away from Lake Cahuilla is controlled by avulsion rather than the elevation of Lake Cahuilla's shoreline. Therefore, even though Lake Cahuilla may be full, the Colorado River may continue to supply sediment to the north for prolonged periods of time. Desiccation observed onshore at higher elevations does not always represent prolonged exposure at lower elevations, nor does it necessarily mean that a component of Colorado River flow did not still enter the basin. These intervals may simply record brief shoreline regressions at higher elevations around the basin (e.g., Coachella site at 3 m below the high-shoreline). For example, high-amplitude layers 2S and 3S appear to have been deposited when the LC shoreline dropped, resulting in basin-ward shift of coarse-grained material, but the deeper portions of the basin remained subaqueous.

Layer 2S thickens south of the hinge zone implying it formed when the Colorado River flow returned and deposited a thick fan delta sequence. Subunits within layers 2S and 4S fluctuate between high- and low-amplitude (Figures 5-7). These fluctuations are interpreted as localized parasequence sets formed during lobe-shifting and infilling of

accommodation that results in along-shore variability between distal (low-amplitude) and proximal (high-amplitude) facies. Offshore imaging reveals at least six additional lake sequences that have not been logged at onshore sites (Philibosian, 2007). Longer paleoseismic records improve our estimates for recurrence intervals as well as fault interaction and distribution of strain. Coring beneath the Salton Sea and/or deeper excavation at the Coachella paleoseismic site to establish a depth transect at different elevations of Lake Cahuilla will provide a comprehensive stratigraphic model for constraining more paleoseismic events.

5.5.2 Earthquakes and Slip-Rates

To constrain the age of fault displacement, we locate the most recent event horizon, then flatten the entire section to that horizon in order to locate older displacement (Figures 8 and 9). Locating the event horizons also involved significant stratigraphic correlation and interpretation to identify onlap and divergence. Identifying event horizons was particularly difficult when offset occurred during high-stand intervals and displacement resulted in slight thickening of the fine-grained facies. Most accommodation was infilled during subsequent floods and coarse-grained deposition. The following measurements were made for faults H7, H8 and H9: (H7) 184 displacement measurements on 21 CHIRP sections, (H8) 16 measurements on 4 sections and (H9) 22 measurements on 4 sections. In total, we identified 25 vertical displacement events across these three faults since layer 14L was deposited.

Recurrence intervals for faults in the southern Salton Sea are relatively short (Table 2; Figures 16 and 17) and are comparable to recurrence estimates on the southern SAF (Philibosian, 2007). H7, H8, H9 and S1 each had events between ~1720 – 1907 that may have occurred around the same time as a number of paleoearthquakes on faults in and around the Salton Sea (Hudnut et al., 1989c; Hudnut and Sieh, 1989; Meltzner et al.,

2006; Philibosian, 2007; Williams et al., 1990). Correlating the onshore events to offshore events is difficult and only a few events appear to be contemporaneous. We performed a detailed investigation of potential correlations, or synchronicity, between events offshore and events at the Coachella SAF site (Figure 18). From oldest to youngest, event *h*, observed on H7, H8 and H9 appears to correlate with event 5 observed on the SAF during flooding of lake 5 (Figures 16 and 17). Event 4 from Philibosian (2007) occurred during 5S may correlate with event *f* observed on H9. Given the best age estimates for onshore event 3 of 1280 and 1300 AD, and its position in the mid-section of 4S, this event does not appear to correlate with offshore event *e* (although this assumes a linear-rate of deposition during sub-aerial exposure). Event *e* is observed on H7, H8, and H9 and appears to occur at ~1360 AD, during lake 3 flooding. Nevertheless, the age estimate for event *e* is within uncertainty of event 3 from the onshore Coachella site. Of the five events observed on all three eastern hinge faults, only two potentially correlate with the onshore SAF events. Based on the youthful nature of the scarp across S2 during event *a* and the absence of overlying sediment drape, the MRE appears to have occurred during the last ~30-50 years. Folding of Salton Sea sediment on fault H7 also suggests recent deformation.

Clearly more investigations are required at different elevations in the basin to evaluate the coincident timing of events. The limited data precludes us from making any predictions about the hinge faults triggering the SAF or vice versa. There is potential for stress interaction between these fault systems (King et al., 1994). Stress triggering of the Superstition Hills Fault by events on cross-faults in the region has been observed (Hudnut et al., 1989b). Assuming strain is released seismically, the length and displacement-per-event on the hinge faults suggest they could produce events of magnitude 6.0-6.8. Simulations of such an event on H7 have shown that static shear stress along the SAF near Bombay Beach (Figure 1) would increase by more than 3 bars (Kilb et al., 2009).

In our tectonic model, the hinge zone faults are accommodating, in large part, the extensional component of deformation and differential subsidence that is occurring in the southern Salton Sea. Consequently, these hinge faults may have a different recurrence interval and may not be coincident with events on the southern SAF. It is important to note, even amongst the hinge faults, events observed on one fault are not observed on adjacent faults, let alone the southern SAF.

Numerous crossings of multiple faults have revealed that the fault systems are complicated and three-dimensional. Paleoseismic studies need to examine multiple faults at different elevations within the Lake Cahuilla system. At this junction it is not possible to determine if the hinge faults trigger the southern SAF and thus control its rupture propagation direction. Despite limited correlation between onshore events and offshore events, the new data reveal a very robust correlation between events on the hinge zone faults and flooding events associated with Colorado River inflow (Figures 9, 16 and 17). The Colorado River appears to also play an important role in modulating the earthquake cycle beneath the Salton Sea (Figures 9, 16 and 17). Rapid loading by sedimentation and water may change the stress conditions in the southern Salton Sea. Paleoearthquakes in the Salton Sea seem to cluster around times when the Colorado River was spilling into a dry basin causing a rapid transition from a subaerial to deep lacustrine environment. The correlation suggests a common process causes these faults to rupture in concert or release strain through clustered seismicity during flooding. Faults may be modulated more heavily by the flooding of the basin than by stress interaction amongst each other. Previous studies have noted similar recurrence intervals between earthquakes on the SAF and Lake Cahuilla high-stands (Luttrell et al., 2007).

Displacement timing in the western hinge-zone is difficult to constrain due to the subtle nature of deformation and absence of definitive event horizons (Figures 11 and 12). A strike-slip component of deformation is likely, but difficult to measure using

two-dimensional profiles. Synclinal folding along faults may be evidence for strike-slip deformation, particularly along faults H8 and H9 (Figures 6 and 7), but the consistency in magnitude and direction of vertical displacement in the hinge zone suggests that extension is the dominant mode of deformation. Slip inversion and fold growth on H9 (Figure 7) may be evidence for a change in kinematics through time from an oblique-convergent to oblique-divergent sense of motion between 14L to 8L. H9 had an abrupt change in kinematics over an ~2,000 year time scale. This observation suggests that the style of deformation has changed quickly through time or faults alternate between different kinematic modes at different time periods.

The relationship between onshore and offshore faults remains poorly understood. Distinct 0.0 - 0.3 m high seafloor scarps along fault S2 and slight folds in Salton Sea sediments across faults S1, S3, and S4 suggest recent displacement. These faults trend ~N10°E and have a consistent down-to-the-southeast sense of slip. The 1987 Elmore Ranch Fault event recorded ~0.15 m of sinistral offset along a ~N40°E plane (Hudnut et al., 1989a; Sipkin, 1989). As the Elmore Ranch Fault enters the SAF-IF step-over its azimuth may adjust to accommodate extension, or these faults may be entirely independent of one another. Further mapping is required to understand the relationship of the southern faults to the Elmore Ranch Fault system. Aseismic creep and triggered slip have been observed on faults surrounding the Salton Sea, including the Extra Fault (Hudnut et al., 1989a; Lohman and McGuire, 2007; Lyons and Sandwell, 2003; Lyons et al., 2002; Meltzner et al., 2006). Some of the seafloor offsets observed, particularly along faults in the western hinge zone that project with the onshore Extra Fault, may be from triggered slip following large events in the region. Although evidence for fault displacement in the Salton Sea during discrete events is definitive, we cannot discount sudden aseismic slip as a possible slip mechanism. Such events have been observed in other extensional settings (Dobre and Peltzer, 2007) and given the high heat flux and

young volcanic activity along the southern shoreline the Salton Sea may be experiencing similar processes.

The late Holocene to present deformation on the hinge-zone faults appears to be predominantly dip-slip in nature. The hinge faults trend approximately 50° oblique to the SAF and show consistent down-to-the-southeast vertical displacement despite minor along-strike jogs and bends. Furthermore, the vertical offset per event and vertical slip-rates are relatively large and thus accommodate a significant percentage of the strain transferred from the SAF to the Imperial Fault (Brothers et al., 2009a). The nearly flat sedimentary horizons deposited by Lake Cahuilla offer little opportunity for strike-slip faults to create topographic relief. To generate 7 m of throw by a strike-slip fault in this environment would require an unrealistic amount of horizontal offset during the given time interval. Nevertheless, we cannot exclude a component of strike-slip along these faults. In Figure 7, for example, fault H9 appears to have a component of strike slip in the region imaged by CHIRP profiles. The confluence of hinge faults and the SAF is expected to produce complicated deformation as strain is transferred between faults systems. Constraining the relative amounts of strike-slip versus dip-slip offset on faults in the Salton Sea requires further study.

Although many of the hinge faults have relatively high slip-rates, southward divergence and rotated beds indicate the basin is bounded by a down-to-the-northwest fault (or system of faults) with a significantly higher slip-rate. Brothers et al. (2009a) inferred subsidence rates up to 20 mm/yr during the last several hundred years. The ~ 10 mm/yr of subsidence across the hinge zone can be converted into ~ 6 mm/yr of horizontal extension (assuming 60° southeast dipping fault plane). In rift basins, between 20-50% of the total extension is typically distributed across secondary faulting in the hinge zone (Morley, 1995) implying between 12 – 30 mm/yr of extension is accommodated south of the hinge. It appears that at least 50% of the 23 mm/yr (Meade and Hager, 2005)

of horizontal slip transferred across the SAF-IF pull-apart basin is accommodated by extension.

Faults discovered north of the hinge zone are poorly constrained and need to be studied further. N2 and N3 have had displacement during the last 2 kyr. Tight synclinal folding across fault N2 implies a large component of strike-slip. N3 may be a minor splay off the nearby SAF, whereas N2 may be a splay off the SAF that trends along the western side of the valley and east edge of the Santa Rosa Mountains. Onshore reconnaissance may improve mapping of these structures and their relationship to faults mapped in Pleistocene and older units (Dibblee, 1984). Farther southeast, fault N1 (Figure 3) is sub-parallel to the SAF and might help explain transpressional folding in Durmid Hill (Burgmann, 1991), although its slip rate appears relatively low.

5.6 CONCLUSIONS

This study has provided the first detailed look at Lake Cahuilla sedimentation and paleoseismic records in the Salton Sea. Future studies aimed at improving the age dating in sea are necessary to constrain the displacement history prior to ~830 AD. Deeper penetrating seismic reflection data will provide important constraints on the longer-term evolution of these faults and how they interact. The most significant results of this study are summarized below.

1. Correlation between high-amplitude reflections in CHIRP profiles and coarse-grained sediment layers in CPT soundings allow us to identify parasequences sets in Lake Cahuilla sediment beneath the Salton Sea. Correlative parasequences have been radiocarbon dated at onshore sites and provide a chronostratigraphic framework for acoustic stratigraphy back to ~830 AD. At least 14 Lake Cahuilla parasequences are observed in the Salton Sea. Not all Lake Cahuilla sequences are separated by desiccation events. Stratigraphic evidence suggests there were extending periods of

- lacustrine conditions that may have experience brief shoreline regressions.
2. Shoreline transgressions caused by Colorado River diversions into the Salton Basin result in rapid deposition that infills tectonically generated accommodation south of the hinge zone. Thick wedges of fan delta facies onlap the hinge zone and diverge southward.
 3. Assuming strain is released seismically, the Salton Sea experiences moderate to large earthquakes every 100 - 200 years and the dominant mode of deformation is extension. Vertical slip rates along individual faults are over 3.4 mm/yr.
 4. Displacement on hinge faults H7-H9 appears coincident with major flooding from the Colorado River. The onset of flooding appears to trigger events on the hinge faults within the sea. Earthquake 5 on the SAF appears to be synchronous with cross fault rupturing event h; earthquake 3 on the SAF appears to have preceded by several decades rupturing of the cross faults during flooding event e, but this asynchronous behavior may not be true, but potentially explained by a rapid infilling of 4S at the Coachella site during the decade or so of rise time to highstand (e.g., storm driven sedimentation).
 5. Given the proximity of these hinge faults to the SAF, static stress changes following displacement, either seismic or aseismic, on offshore faults may alter stress conditions along the southernmost SAF and promote a destructive northward propagating rupture (Olsen et al., 2006). Their roles as stress modulators need to be addressed by future research.

5.7 ACKNOWLEDGEMENTS

This work was funded by the State of California Department of Water Resources, Scripps Institution of Oceanography, UC Academic Senate, National Science Foundation (grants OCE-0112058 and EAR-0545250) and the Southern California Earthquake Center

(grant 2008-08127). We would like to thank the Sonny Bono Salton Sea National Wildlife Refuge and the Salton Sea State Recreation Area for their hospitality and providing access to their facilities during data collection. We would also like to thank E. Aaron, L. Johnstone, J. McCullaugh, J. Dingler and numerous others for field assistance.

The text and figures from this chapter are being prepared for publication in: Brothers, D.S., Driscoll, N.W., Kent, G.M., Harding, A.J., Babcock, J.M, and Baskin, R.L., In Prep, Late Holocene earthquake and sedimentary history beneath the Salton Sea, Southern California. The dissertation author was the primary researcher and author of the submitted work. The co-authors directed and supervised that research, which forms the basis for this chapter.

5.8 REFERENCES

- Becker, T.W., Hardebeck, J.L., and Anderson, G., 2005, Constraints on fault slip rates of the southern California plate boundary from GPS velocity and stress inversions: *Geophysical Journal International*, v. 160, p. 634-650.
- Behr, W., Hudnut, K., Platt, J., Kendrick, K., Sharp, W., Fletcher, K., Finkel, R., and Rood, D., 2007, A revised slip rate estimate for the Mission Creek–Coachella Valley strand of the southern San Andreas fault at Biskra Palms Oasis, Indio, California: southern California Earthquake Center Annual Meeting, Proceedings with Abstracts, v. 17.
- Brothers, D.S., Driscoll, N.W., Kent, G.M., Harding, A.J., Babcock, J.M., and Baskin, R.L., 2009a, Tectonic evolution of the Salton Sea inferred from seismic reflection data: *Nature Geoscience*.
- Brothers, D.S., Kent, G.M., Driscoll, N.W., Smith, S.B., Dingler, J.A., Harding, A.J., Seitz, G.G., Karlin, R., and Babcock, J.M., 2009b, New constraints on earthquake history and slip-rates on the West Tahoe-Dollar Point Fault, Lake Tahoe Basin, CA: *Bulletin of the Seismological Society of America*.
- Bull, J.M., Minshull, T.A., Mitchell, N.C., Thors, K., Dix, J.K., and Best, A.I., 2003, Fault and magmatic interaction within Iceland's western rift over the last 9 kyr: *Geophysical Journal International*, v. 154, p. F1-F7.
- Burgmann, R., 1991, Transpression Along the Southern San-Andreas Fault, Durmid Hill, California: *Tectonics*, v. 10, p. 1152-1163.
- Danforth, W.W., 1997, Xsonar/ShowImage: A Complete System for Rapid Sidescan-Sonar Processing and Display: U.S. Geological Survey Open-File Report, v. 97-686, p. 99.
- Dibblee, T.W., 1984, Stratigraphy and tectonics of the San Felipe Hills, Borrego Badlands, Superstition Hills and vicinity: *Imperial Basin- Tectonics, Sedimentation and Thermal Aspects*; Society of Economic Paleontologists and Mineralogists, p. 31-44.
- Dobre, C., and Peltzer, G., 2007, Fluid-controlled faulting process in the Asal Rift, Djibouti, from 8 yr of radar interferometry observations: *Geology*, v. 35, p. 69-72.

- Fay, N.P., and Humphreys, E.D., 2005, Fault slip rates, effects of elastic heterogeneity on geodetic data, and the strength of the lower crust in the Salton Trough region, southern California: *Journal of Geophysical Research-Solid Earth*, v. 110, p. -.
- Fialko, Y., 2006, Interseismic strain accumulation and the earthquake potential on the southern San Andreas fault system: *Nature*, v. 441, p. 968-971.
- Fletcher, K.E., Sharp, W.D., Kendrick, K.J., and Hudnut, K., 2007, U-Series ages for the Biskra Palms alluvial fan and their implications for long-term slip-rate of the Coachella Valley segment of the San Andreas Fault, Southern California: *GSA Annual Meeting*, Paper No. 123-5.
- Fumal, T.E., Rymer, M.J., and Seitz, G.G., 2002, Timing of large earthquakes since AD 800 on the Mission Creek strand of the San Andreas fault zone at Thousand Palms Oasis, near Palm Springs, California: *Bulletin of the Seismological Society of America*, v. 92, p. 2841-2860.
- Hudnut, K., Seeber, L., Rockwell, T., Goodmacher, J., Klinger, R., Lindvall, S., and Mcelwain, R., 1989a, Surface Ruptures on Cross-Faults in the 24 November 1987 Superstition Hills, California, Earthquake Sequence: *Bulletin of the Seismological Society of America*, v. 79, p. 282-296.
- Hudnut, K.W., Seeber, L., and Pacheco, J., 1989b, Cross-Fault Triggering in the November 1987 Superstition Hills Earthquake Sequence, Southern-California: *Geophysical Research Letters*, v. 16, p. 199-202.
- Hudnut, K.W., Seeber, L., and Rockwell, T., 1989c, Slip on the Elmore Ranch Fault during the Past 330 Years and Its Relation to Slip on the Superstition Hills Fault: *Bulletin of the Seismological Society of America*, v. 79, p. 330-341.
- Hudnut, K.W., and Sieh, K.E., 1989, Behavior of the Superstition Hills Fault during the Past 330 Years: *Bulletin of the Seismological Society of America*, v. 79, p. 304-329.
- Kendrick, K.J., Morton, D.M., Wells, S.G., and Simpson, R.W., 2002, Spatial and temporal deformation along the northern San Jacinto fault, southern California: Implications for slip rates: *Bulletin of the Seismological Society of America*, v. 92, p. 2782-2802.

- Kent, G.M., Babcock, J.M., Driscoll, N.W., Harding, A.J., Dingler, J.A., Seitz, G.G., Gardner, J.V., Mayer, L.A., Goldman, C.R., Heyvaert, A.C., Richards, R.C., Karlin, R., Morgan, C.W., Gayes, P.T., and Owen, L.A., 2005, 60 k.y. record of extension across the western boundary of the Basin and Range province: Estimate of slip rates from offset shoreline terraces and a catastrophic slide beneath Lake Tahoe: *Geology*, v. 33, p. 365-368.
- Kilb, D., Brothers, D.S., Lin, G.Q., Kent, G.M., Newman, R., and Driscoll, N.W., 2009, On The Dichotomy Between Geologic And Seismologic Signatures in Data From the Salton Sea Region in Southern California Southern California Earthquake Center Annual Meeting, v. Proceedings and Abstracts.
- King, G.C.P., Stein, R.S., and Lin, J., 1994, Static Stress Changes and the Triggering of Earthquakes: *Bulletin of the Seismological Society of America*, v. 84, p. 935-953.
- Lamarche, G., Barnes, P.M., and Bull, J.M., 2006, Faulting and extension rate over the last 20,000 years in the offshore Whakatane Graben, New Zealand continental shelf: *Tectonics*, v. 25, p. -.
- Lohman, R.B., and McGuire, J.J., 2007, Earthquake swarms driven by aseismic creep in the Salton Trough, California: *Journal of Geophysical Research-Solid Earth*, v. 112, p. -.
- Luttrell, K., Sandwell, D., Smith-Konter, B., Bills, B., and Bock, Y., 2007, Modulation of the earthquake cycle at the southern San Andreas fault by lake loading: *Journal of Geophysical Research-Solid Earth*, v. 112, p. -.
- Lyons, S., and Sandwell, D., 2003, Fault creep along the southern San Andreas from interferometric synthetic aperture radar, permanent scatterers, and stacking: *Journal of Geophysical Research-Solid Earth*, v. 108, p. -.
- Lyons, S.N., Bock, Y., and Sandwell, D.T., 2002, Creep along the imperial fault, southern California, from GPS measurements: *Journal of Geophysical Research-Solid Earth*, v. 107, p. -.
- McHugh, C.M.G., Seeber, L., Cormier, M.H., Dutton, J., Cagatay, N., Polonia, A., Ryan, W.B.F., and Gorur, N., 2006, Submarine earthquake geology along the North Anatolia Fault in the Marmara Sea, Turkey: A model for transform basin sedimentation: *Earth and Planetary Science Letters*, v. 248, p. 661-684.

- Meade, B.J., and Hager, B.H., 2005, Block models of crustal motion in southern California constrained by GPS measurements: *Journal of Geophysical Research-Solid Earth*, v. 110, p. -.
- Meltzner, A.J., Rockwell, T.K., and Owen, L.A., 2006, Recent and Long-Term Behavior of the Brawley Fault Zone, Imperial Valley, California: An Escalation in Slip Rate?: *Bulletin of the Seismological Society of America*, v. 96, p. 2304-2328.
- Morley, C.K., 1995, Developments in the structural geology of rifts over the last decade and their impact on hydrocarbon exploration: From Lambiase, J.J. (ed), *Hydrocarbon Habitat in Rift Basins*, Geological Society Special Publications, v. 80, p. 1-32.
- Olsen, K.B., Day, S.M., Minster, J.B., Cui, Y., Chourasia, A., Faerman, M., Moore, R., Maechling, P., and Jordan, T., 2006, Strong shaking in Los Angeles expected from southern San Andreas earthquake: *Geophysical Research Letters*, v. 33, p. -.
- Philibosian, B., 2007, Paleoseismology of the San Andreas Fault at Coachella, California: Master's Thesis, University of Oregon.
- Pratson, L., Hughes-Clarke, J., Anderson, M., Gerber, T., Twichel, D., Ferrari, R., Nittrouer, C., Beaudoin, J., Granet, J., and Crockett, J., 2008, Timing and patterns of basin infilling as documented in Lake Powell during a drought: *Geology*, v. 36, p. 843-846.
- Robertson, P.K., 1990, Soil Classification Using the Cone Penetration Test: *Canadian Geotechnical Journal*, v. 27, p. 151-158.
- Rockwell, T., Loughman, C., and Merifield, P., 1990, Late Quaternary Rate of Slip Along the San-Jacinto Fault Zone near Anza, Southern California: *Journal of Geophysical Research-Solid Earth and Planets*, v. 95, p. 8593-8605.
- Schroeder, R.A., Orem, W.H., and Kharaka, Y.K., 2002, Chemical evolution of the Salton Sea, California: nutrient and selenium dynamics: *Hydrobiologia*, v. 473, p. 23-45.
- Sieh, K.E., and Williams, P.L., 1990, Behavior of the Southernmost San-Andreas Fault during the Past 300 Years: *Journal of Geophysical Research-Solid Earth and Planets*, v. 95, p. 6629-6645.

- Sipkin, S.A., 1989, Moment-Tensor Solutions for the 24 November 1987 Superstition Hills, California, Earthquakes: Bulletin of the Seismological Society of America, v. 79, p. 493-499.
- URS, 2004, Preliminary in-sea geotechnical investigation, Salton Sea Resoration Project Report, Riverside and Imperial Counties, California, p. 399.
- Van De Kamp, P.C., 1973, Holocene Continental Sedimentation in Salton-Basin, California - Reconnaissance: Geological Society of America Bulletin, v. 84, p. 827-848.
- Van Wagoner, J.C., and Bertram, G.T., 1995, Sequence Stratigraphy of Foreland Basin Deposits: Tulsa, American Association of Petroleum Geologists, 453 p.
- Williams, P.L., Sykes, L.R., Nicholson, C., and Seeber, L., 1990, Seismotectonics of the Easternmost Transverse Ranges, California - Relevance for Seismic Potential of the Southern San-Andreas Fault: Tectonics, v. 9, p. 185-204.

Table 1: Onshore-Offshore Chronostratigraphic Correlation						
Layer	<u>Coachella Site (9 m elevation)</u>			<u>Seafloor (-85 m elevation)</u>		
	Depositional Interval (Calendar Date AD)		Duration (years)	Depositional Interval (Calendar Date AD)		Duration (years)
SS	N/A	N/A	N/A	1907	present	100
1S	Present	1720	290	1907	1720	190
1L	1720	1650	70	1720	1630	90
2S	1650	1620	30	Regression, but no desiccation		
2L	1620	1480	140	1680	1460	220
3S	1480	1460	20	Regression, but no desiccation		
3L	1460	1380	80	1520	1360	160
4S	1380	1200	180	1360	1260	100
4L	1200	1150	50	1260	1130	130
5S	1150	1000	150	1130	1060	70
5L	1000	?	?	1060	?	?
6S	?	?	?	?	?	?
6L	?	850	150	?	830	230
7S	850	?	?	830	?	?

*Assume 20 years are required to fill the lake to 13 m and at a desiccation rate of 1.8 m/yr, ~60 years are required to dry lake.
**1770 younger bound on 1L and 1720 older bound on 1S are based on reports from the 1770 Anza expedition, in which no lake existed in the basin (Philibosian, 2007).

Table 5-1: Lake Cahuilla flooding and desiccation cycles from Philibosian (2007). Offshore parasequences are expected to represent longer subaqueous intervals due to an ~60-year time difference between desiccation at 9m and potential desiccation deeper in the basin. The chronostratigraphic model represents the time required to deposit each layer based on radiocarbon dates and the estimated ages have significant uncertainty (see Philibosian, 2007).

Table 5-2: Paleoearthquake offset and timing estimates. n represents the number of measurements. The timing estimates are based on the chronostratigraphic model presented in Table 1. Age bounds incorporate the total uncertainty for each given depositional unit at the Coachella site. Best estimates extrapolate a narrower age range based on the positioning of the event within a given stratigraphic unit.

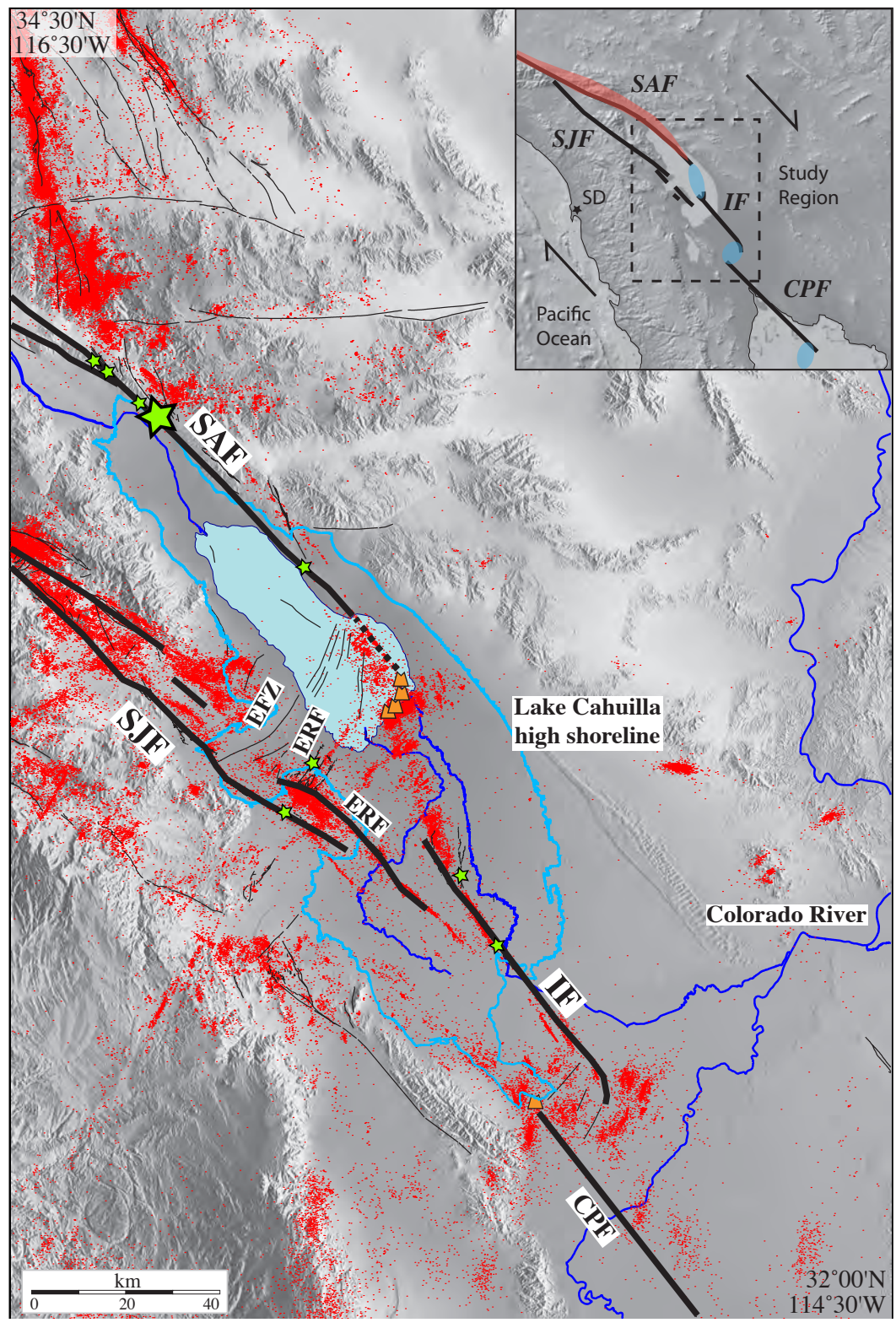
Table 2. Earthquake Measurements: Offset and Timing Estimates

	Event	Layer	n	Mean offset (m)	Age Bounds (Year AD)*	Preferred Age (Year AD)	Comment
Fault: H7	a	SS	21	0.4 ± 0.2	1907 - 2006	Post 1980	Recent SS offset, seafloor folding
	b	1S	21	0.5 ± 0.2	1680 - 1905	1720 - 1905	Likely after subaerial deposition in 1S
	d	3L	21	0.8 ± 0.3	1380 - 1460	1430 - 1460	Upper third of 3L
	e	4S/3F	19	1.0 ± 0.2	1260 - 1380	1360 - 1380	During 3L flooding
	g	5L	19	0.6 ± 0.1	950 - 1060	970 - 1060	Mid section of 5L
	h	6S/5F	15	0.7 ± 0.1	830 - 1060	900 - 930	During 5L flooding
	i	8L	18	0.7 ± 0.2	?	?	Mid-section of 8L
	j	9S/8F	18	0.5 ± 0.3	?	?	During 8L flooding
	k	10L	16	0.8 ± 0.2	?	?	Later half of 10L
	l	11L	16	0.8 ± 0.2	?	?	Early part of 11L
Fault: H8	b	1S	4	0.3 ± 0.1	1680 - 1907	1720 - 1800	Early part of 1S
	e	4S/3F	4	0.5 ± 0.2	1260 - 1380	1360 - 1380	During 3L flooding
	h	6S/5F	4	0.3 ± 0.2	830 - 1060	900 - 930	During 5L flooding
	j	9S/8F	4	0.5 ± 0.1	?	?	During 8L flooding
	l	11L		0.5 ± 0.1	?	?	Within 11L
Fault: H9	b	1S	4	0.5 ± 0.2	1680 - 1905	1720 - 1905	Likely after subaerial deposition
	c	2L	4	0.5 ± 0.1	1480 - 1620	1480 - 1520	Early part of 2L
	e	4S/3F	4	0.6 ± 0.1	1260 - 1380	1360 - 1380	Later part of 4S, during flooding into 3L
	f	4L	3	0.9 ± 0.1	1150 - 1200	1130 - 1180	Early third of 4L
	g	5L	1	0.2 ± 0.1	950 - 1060	970 - 1060	Mid-section 5L
	h	6S/5F	1	0.4 ± 0.1	830 - 1060	850 - 950	Early 6S or upper 6L
	i	8L	2	0.1 ± 0.1	?	?	Mid-section of 8L
	j	9S/8F	2	-0.3 ± 0.2	?	?	During 8L flooding
	l	11L	1	-0.5 ± 0.1	?	?	Mid section of 11L
	m	13L	1	-0.4 ± 0.1	?	?	Mid section of 13L
	a	SS	15	0.4 ± 0.1	1907 - 2006	Post 1980	Well-defined seafloor scarp
	b	1S	10	0.4 ± 0.1	1680 - 1905	1720 - 1905	Appears to be within 1S

Table 3: Subsidence Rates				
<u>Horizon</u>	<u>Approx. Age (years)</u>	<u>Profile</u>	<u>Differential Subsidence</u>	<u>Subsidence Rate (mm/yr)</u>
3L	650	A	4.1	6.3
3L	650	B	6.7	10.3
6L	1180	A	11.4	9.7
8L	?	A	13.4	?
*Age is given as years before 2010, contrary to convention, because sedimentation has continued to present.				

Table 5-3: Subsidence rates across profiles shown in Figure 15.

Figure 5-1: Regional map of the Salton Trough. Map units: active faults (black lines), seismicity since 1983 (red dots; Lin et al., 2007), selected paleoseismic sites (red stars), Coachella Paleoseismic site from Philibosian (2007; large red star), volcanoes (orange craters). The Lake Cahuilla high shoreline (light blue) and the Salton Sea occupy the northern trough, separated from the Gulf of California by the Colorado River delta. Inset (B): plate boundary schematic of the transition between transpression the San Andreas Fault (SAF) system (red shades) and transtension of the Gulf of California rifted margin (pull-apart basins shaded blue). The Salton Sea covers part of the pull-apart basin formed at a step-over between the SAF and Imperial Fault (IF). Abbreviations: San Jacinto Fault, SJF; Extra Fault Zone, EFZ; Elmore Ranch Fault, ERF; Cerro Prieto Fault, CPF; SD, San Diego.



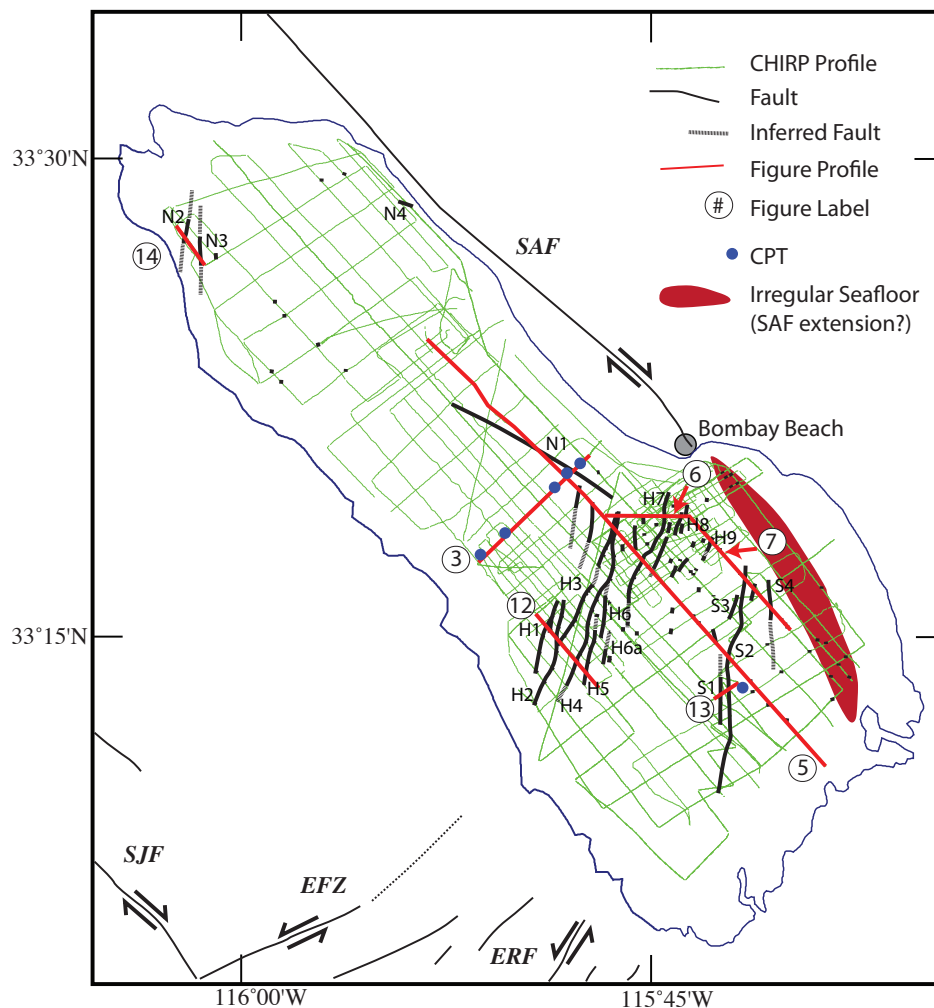
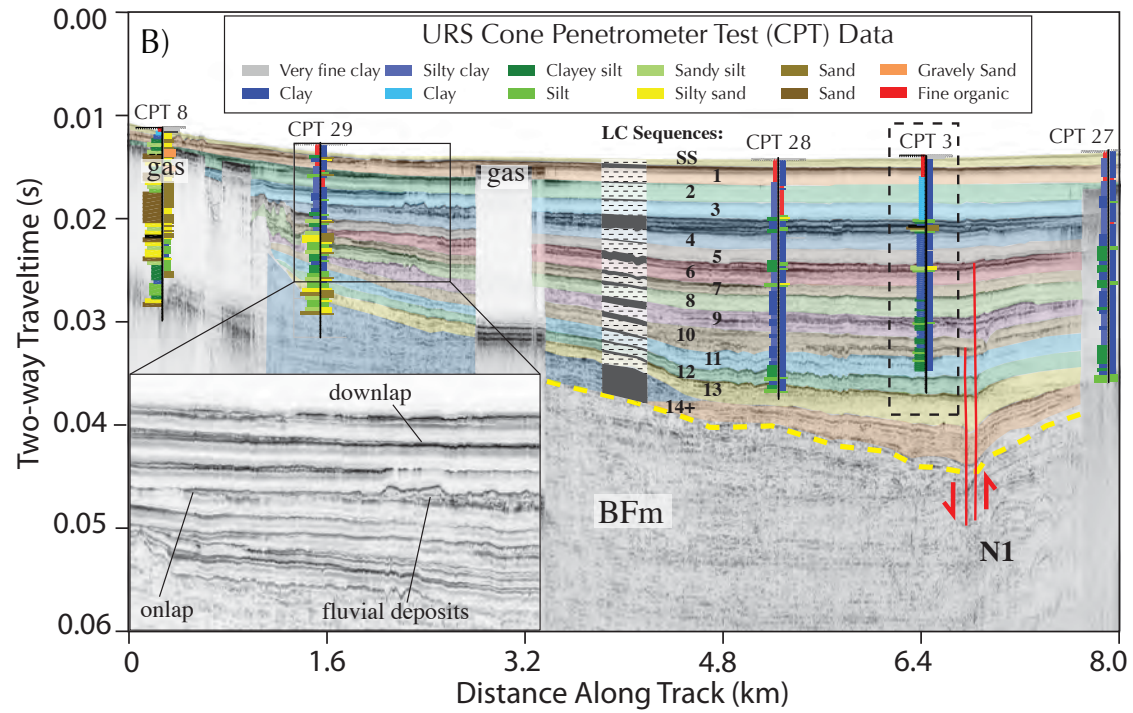
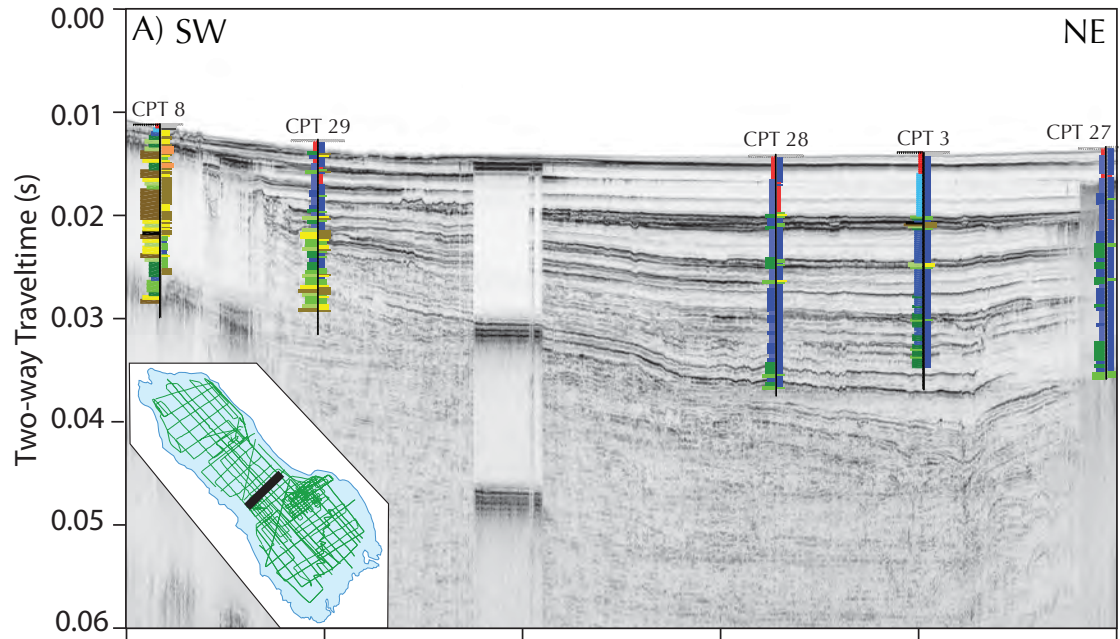


Figure 5-2: Survey map. Over 1,000 line-km of seismic CHIRP data were acquired between 2006 - 2009. Faults discovered in this study are labeled according to their geographic and/or structural position. “H” faults are considered part of the tectonic hinge-zone that bounds extension in the southern half of the Salton Sea (Brothers et al., 2009a). Southern (“S”) and northern (“N”) faults were also identified in sub-bottom sediments. Cone penetration test (CPT) data are from URS (2004) and were used to ground-truth sedimentary horizons imaged in seismic profiles. The (red) shaded region denotes a region of irregular seafloor topography and fluid venting. Numerous craters, pock marks and scarps in this region and may be related to the southernmost extension of the SAF. CHIRP profiles in forthcoming figures are numbered denoted as red lines.

Figure 5-3: Type section used to define Lake Cahuilla chronostratigraphy. A) Uninterpreted CHIRP profile with cone penetration test (CPT) logs superimposed on acoustic horizons. Inset shows location (thick black line). CPT logs contain two columns separated by vertical black lines. On the left is soil behavior type (SBT) and the right is normalized SBT. Normalized cone data (right column) account for increasing overburden stress with depth as measured by pore pressure changes (Robertson, 1990). Overall, both columns at each site reveal similar trends. CPTs show increased sand components moving shoreward, which that correlates with increased acoustic reflectivity in CHIRP profiles. B) Interpreted profile with CPT color key. Inset shows enlarged CHIRP section highlighting onlapping and downlapping coarse grained facies. Downlap records locally sourced sediment from ephemeral streams and fan deltas. Colors represent Lake Cahuilla sedimentary sequences and each sequence is number from 1-14. Stippled column highlights the high-stand (white with dashed lines) from low-stand and fan delta material (gray shaded layers). High-amplitude layers are interpreted as containing both coarse-grained low-stand deposits and fluvial fan-delta deposits associated with Colorado River flooding. Distinguishing between the two is difficult (see text). Dashed box is enlarged section in Figure 5. Dashed brown line marks the approximate boundary between Holocene Lake Cahuilla section (CFm) and Pleistocene (?) Brawley Formation (BFm). Folded strata along fault N1 (red lines) are observed in the CFm and BFm. Dashed box is section shown in Figure 4.



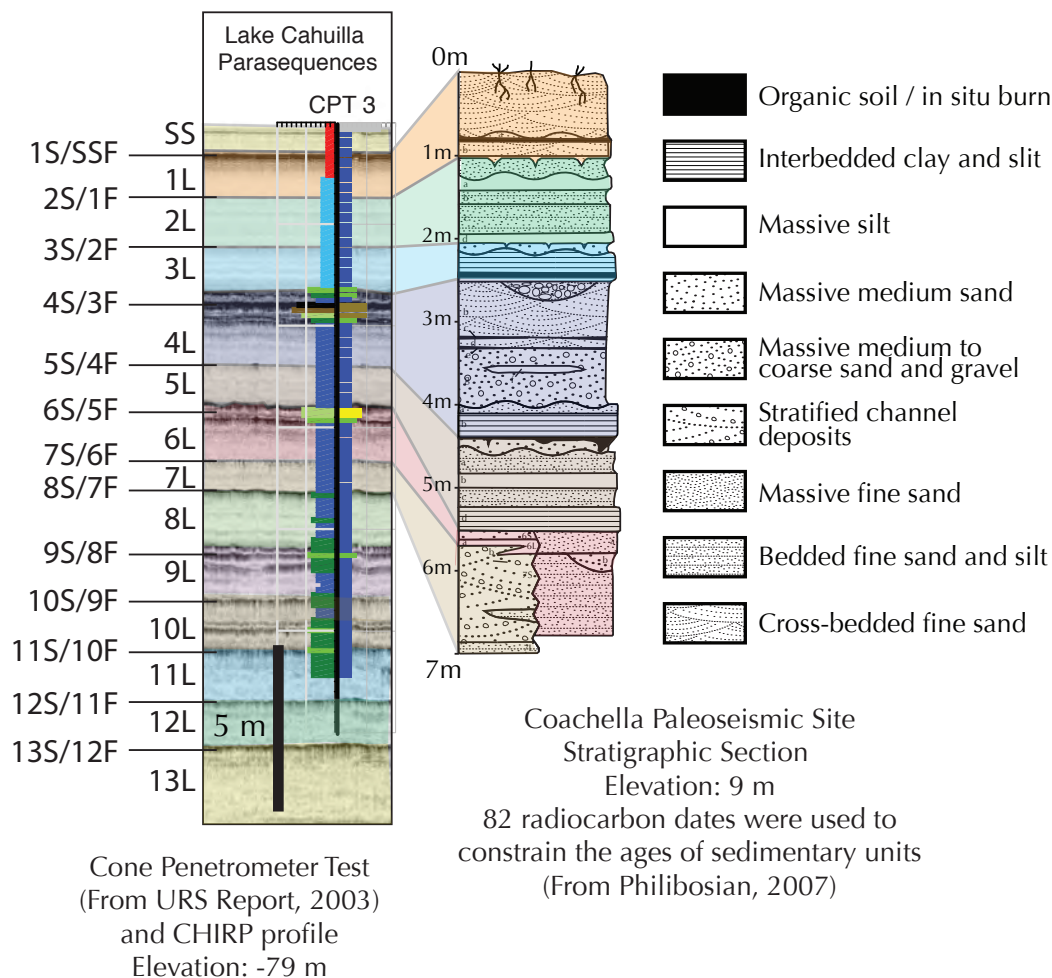


Figure 5-4: Chronostratigraphic correlations between seismic and lithostratigraphy in the Salton Sea and radiocarbon dated Lake Cahuilla sediments at the Coachella Paleoseismic site. Onshore stratigraphic column (right) is modified from Philibosian (2007). Within each Lake Cahuilla sequence, high stand deposits are labeled “L” and lowstand/flood deposits are labeled “S/F”. Fine grained, low amplitude layers 1L, 2L and 3L are separated by relatively thin 2S/1F and 3S/2F layers. CPT soundings detect 2S/1F, 3S/2F and 5S/4F as distinct silt/sand layers closer to the shoreline (Figure 3), but they are not detected by CPTs at this location. Philibosian (2007) defined 4S onshore as a thick accumulation of fluvial and aeolian deposits that was deposited during prolonged subaerial exposure. Offshore, 4S/3F is also a distinct marker bed characterized by high reflectivity and sand/silt components. 6S/5F is the oldest layer that can be correlated to onshore deposits. See Table 1 for lake chronology.

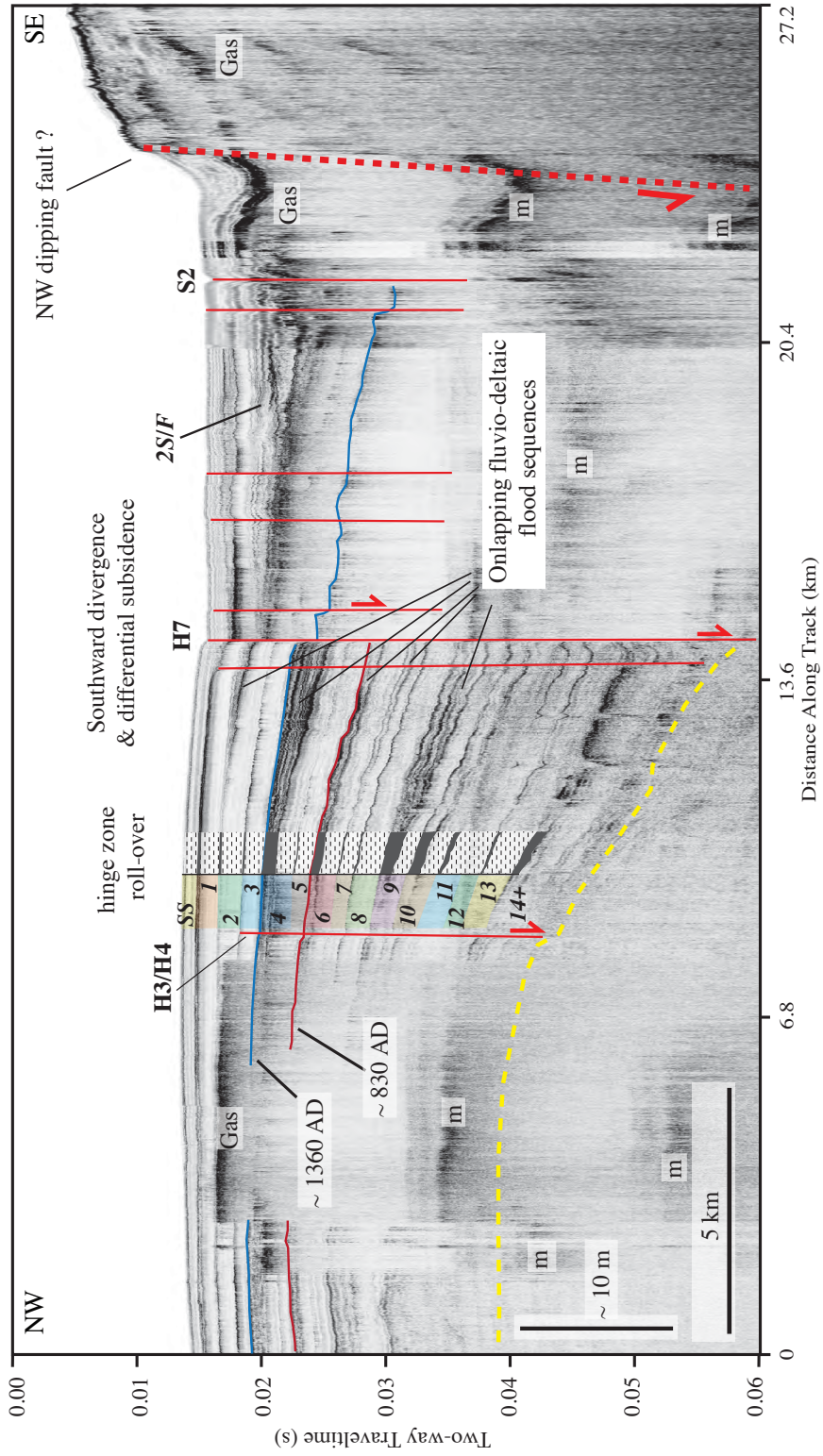


Figure 5-5: Profile spanning the tectonic hinge-zone and southern Salton Sea extension. Stratigraphy diverges south of the hinge, infilling differential subsidence and accommodation along an inferred down-to-the northwest normal fault system (Brothers et al., 2009a). Gas charged sediments limits penetration south of fault H7, but the 4S surface appears to continue to diverge (dark cyan).

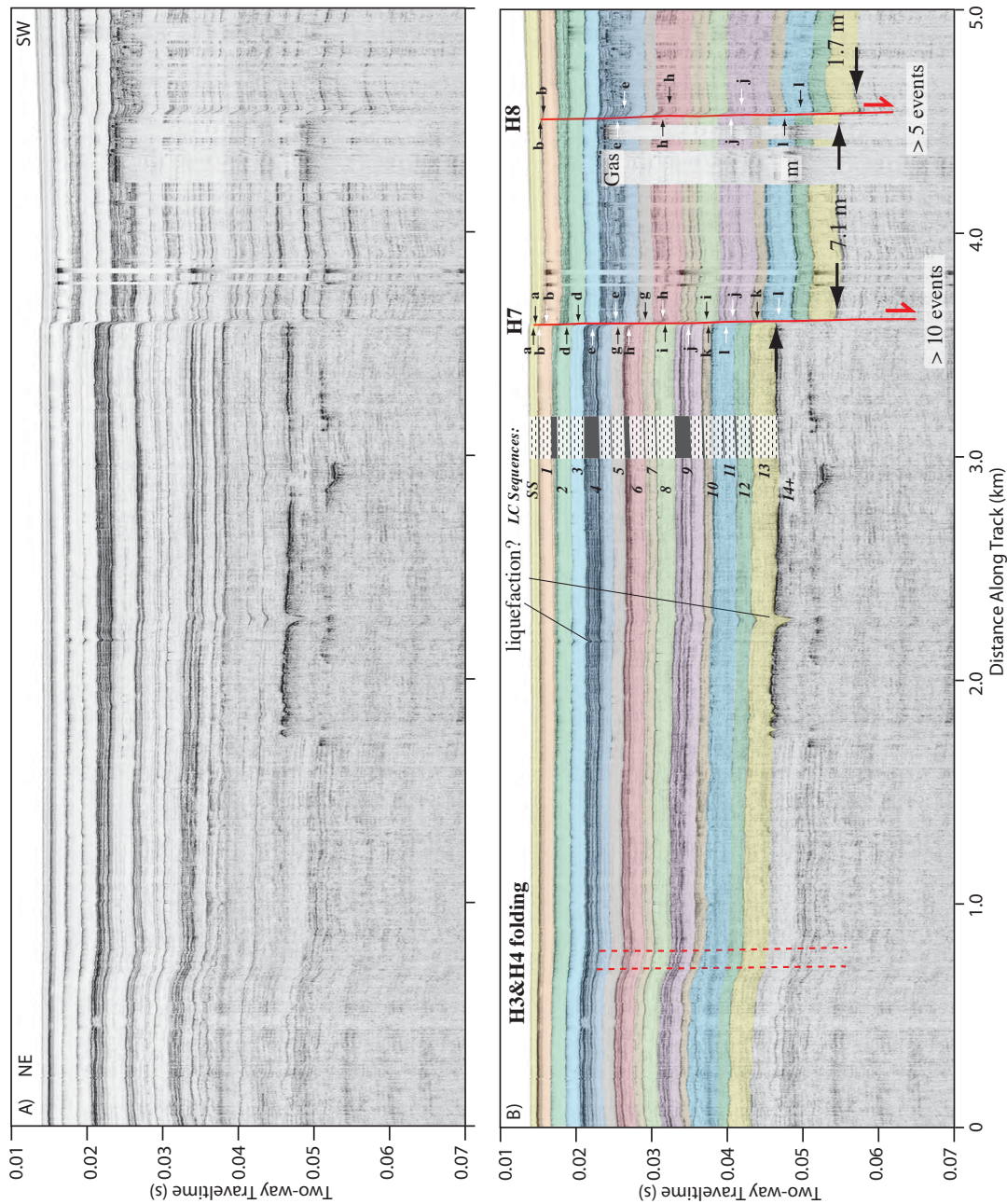


Figure 5-6: Type section over faults H7 and H8. More than ten events are identified along H7 and five on H8 based on growth patterns. Large black arrows denote cumulative offset across the base of 13L. Alternating white and black arrows point to event horizons on the footwall and hangingwall. Earthquakes with the same lettering on separate faults appear to have occurred within the same stratigraphic interval. See Table 2 for earthquake timing and offset measurements.

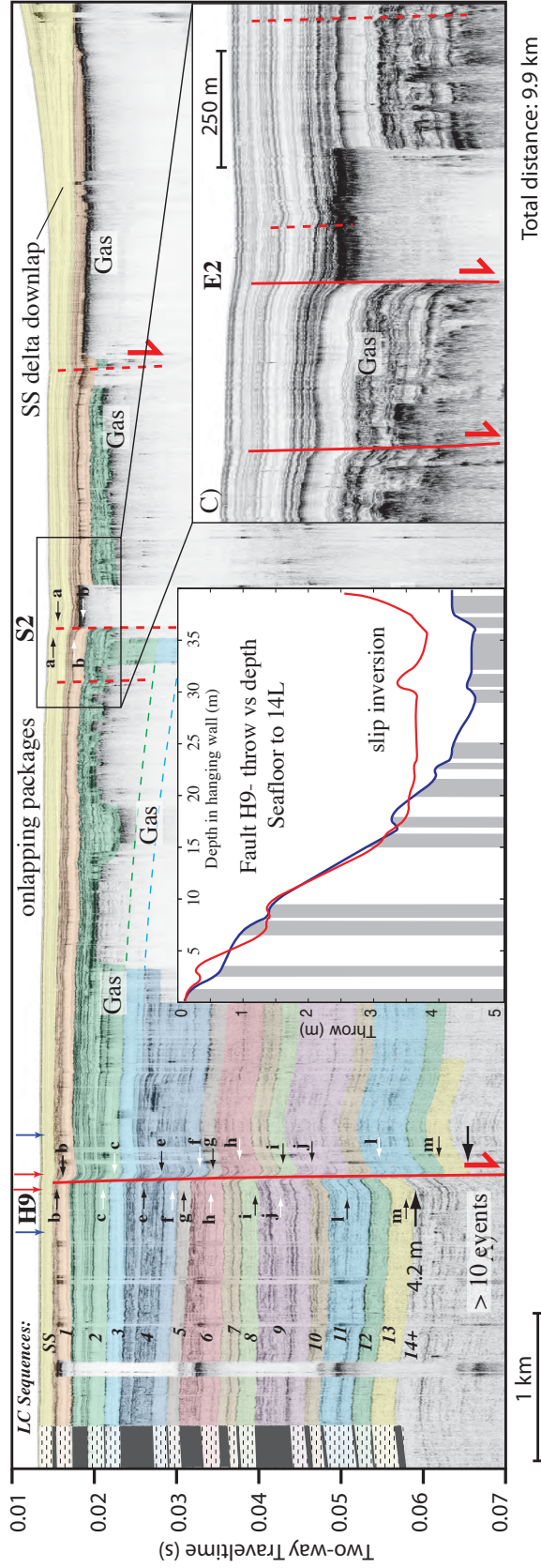
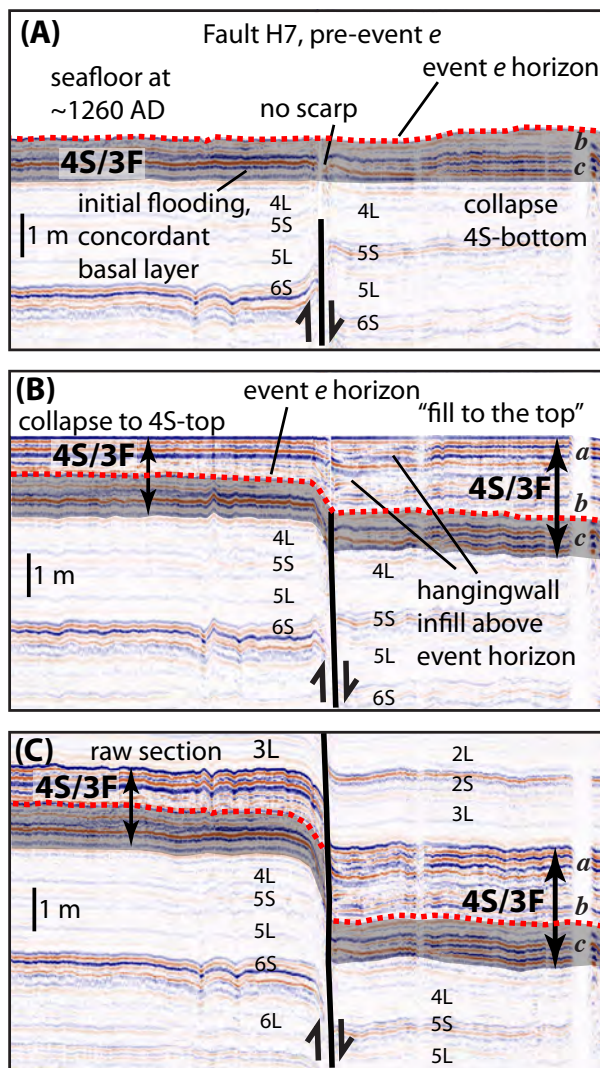


Figure 5-7: Type section of southern sea highlighting faults H9 and S2. Alternating white and black arrows point to event horizons on the footwall and hangingwall from which displacement-per-event estimates were made. Despite the limited penetration due to gas-charged sediment, the top of parasequence 1 (orange layer) has a southward dip at the end of the line, suggesting that rapid subsidence and southward divergence continues beneath the gas-prone sediment. (B) Throw versus depth plot highlighting the fold growth and slip inversion on fault H9 below Lake Cabuilla sequence 7, which may be indicative of strike-slip motion and/or a change from oblique-convergent to oblique-divergent deformation. White and gray shades represent lowstand/flood and highstand deposits, respectively. The blue and red lines correspond to the location of throw and depth measurements relative to the fault. The red profile was measured within 50 m of the fault plane (red arrows at top of CHIRP profile) and the blue profile was measured ~200 m away from the fault on either side. (C) Enlarged section of fault S2. The most recent event occurred within the Salton Sea time period (last 100 years). Gas termination at the fault suggests fault planes provide fluid migration pathways.

Figure 5-8: Enlarged section across fault H7 (Figure 6) to highlight displacement and sedimentary infill during 3S flooding. (A) Stratigraphic section prior to event *e* (dashed red-line). Layer 4S had been deposited (basal high-amplitude unit) and Lake 3 had begun to fill, depositing subunits 4S/3F-c and -b (See Figure 6). Hanging wall growth and/or onlap are not observed below the event horizon. (B) End of lake 3 flooding and coarse-grained deposition. Note the hangingwall onlap and thickening in 4S/3F-a,b that infilled accommodation that formed during event *e*. (C) Raw section representing present-day stratigraphy. Cumulative throw across event *e* horizon represents cumulative throw from events *a-e*. Based on the estimated amount of time required to fill Lake Cahuilla during Colorado River diversions and modern sedimentation rates in the Colorado River delta at Lake Powell (Pratson et al., 2008), the flood deposits may accumulate as quickly as 20 years.



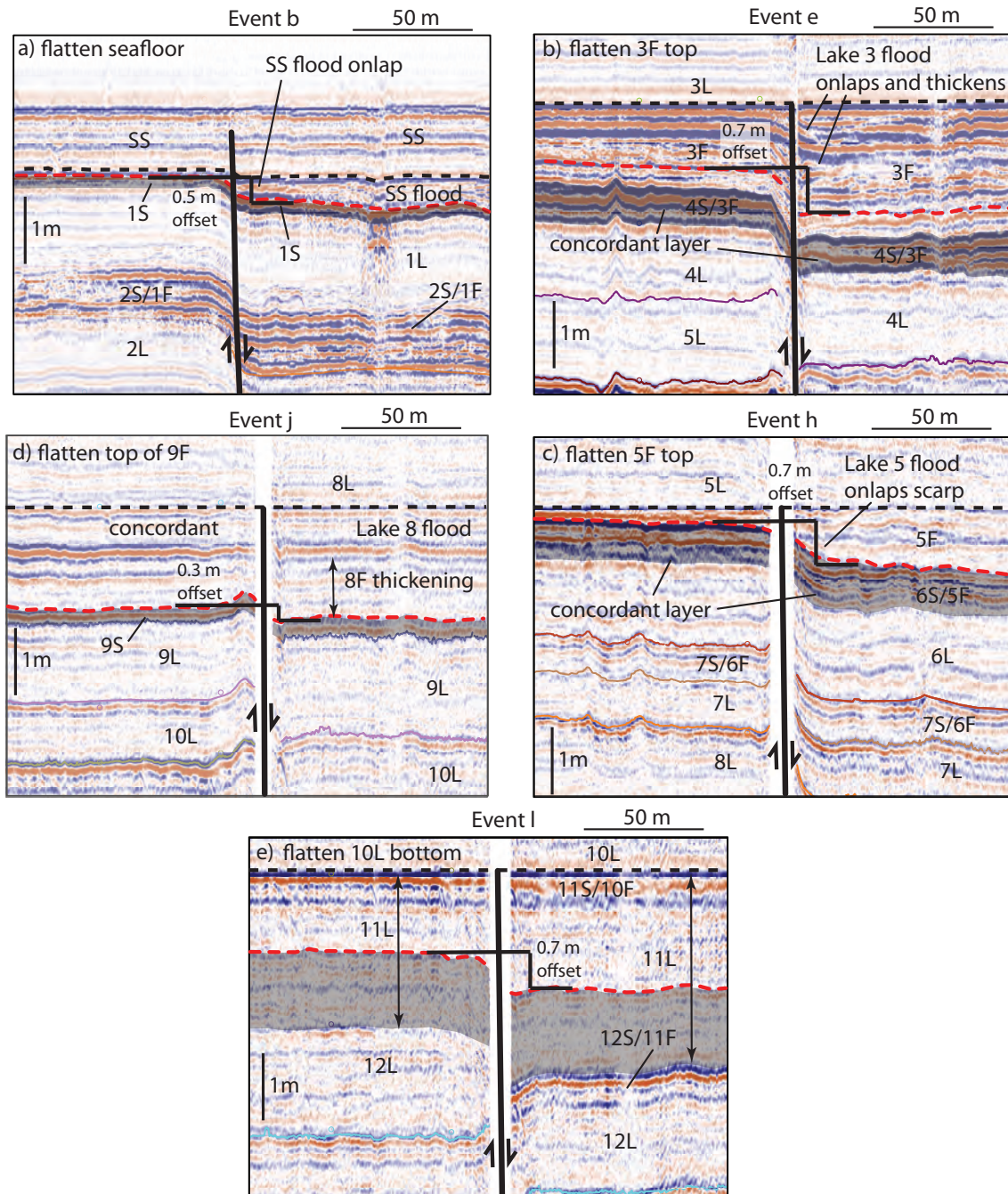


Figure 5-9: Example sections across fault H7 illustrating evidence for events *b*, *e*, *h*, *j*, and *l*. Each of these events is observed on faults H7, H8 and H9. Event *b* is also observed on faults S1 and S2. Based on the stratal geometry and acoustic character, events *b*, *e*, *h*, and *j* appear to have occurred during flooding episodes. Event *l* occurred during prolonged high-stand episode 11L.

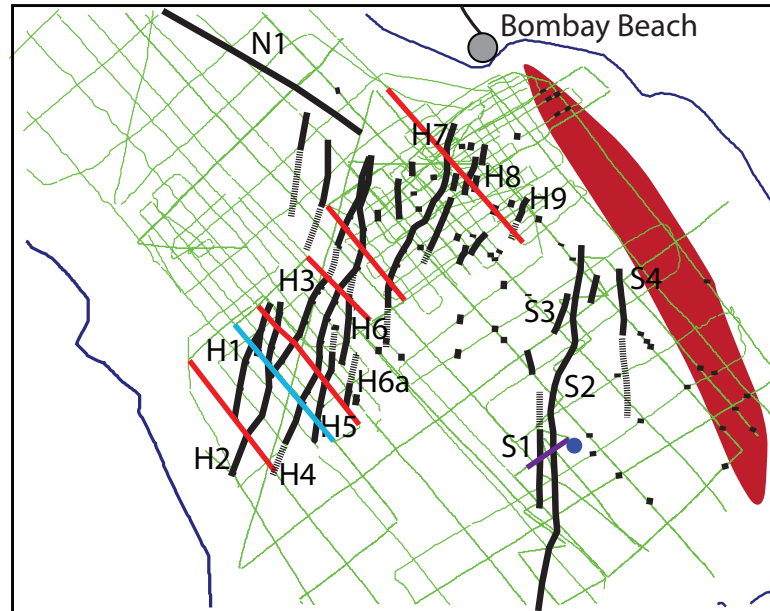
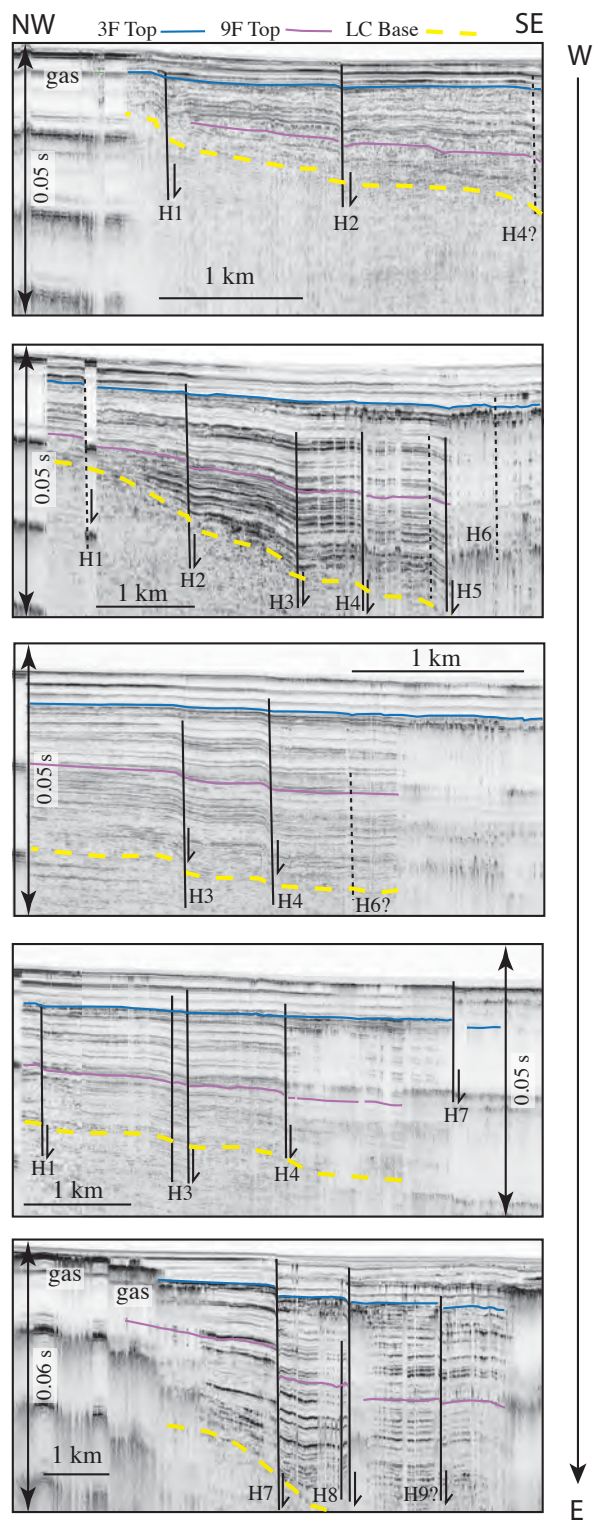


Figure 5-10: Location map for CHIRP profiles in Figures 11, 12 and 13. Red lines represent profiles shown in Figure 11. The Blue line over faults H1-H5 is shown in Figure 12 and the purple line over faults S1 and S2 is shown in Figure 13.

Figure 5-11: Panel of CHIRP profiles across hinge zone faults illustrating the structural variation from west (top) to east (bottom). Vertical exaggeration is not fixed between profiles. Fault segments and profile locations are shown in Figures 2 and 10. Colored lines highlight marker beds: 4S top (blue; 1360 AD) and 9S (Purple; age unknown). Faults to the west have less throw and do not exhibit the distinctive growth patterns seen along faults to the east. Subsidence is observed to increase from west to east as faults extend into the SAF-IF extensional step-over (Figure 1). Deformation in the western panels is expressed as subtle down-to-the-southeast monocline folds whereas deformation in the east is expressed as distinct faulting and vertically offset horizons. Minor deformation observed in Salton Sea sediments may be related to triggered slip observed on faults west of the Salton Sea (Hudnut et al., 1989a).



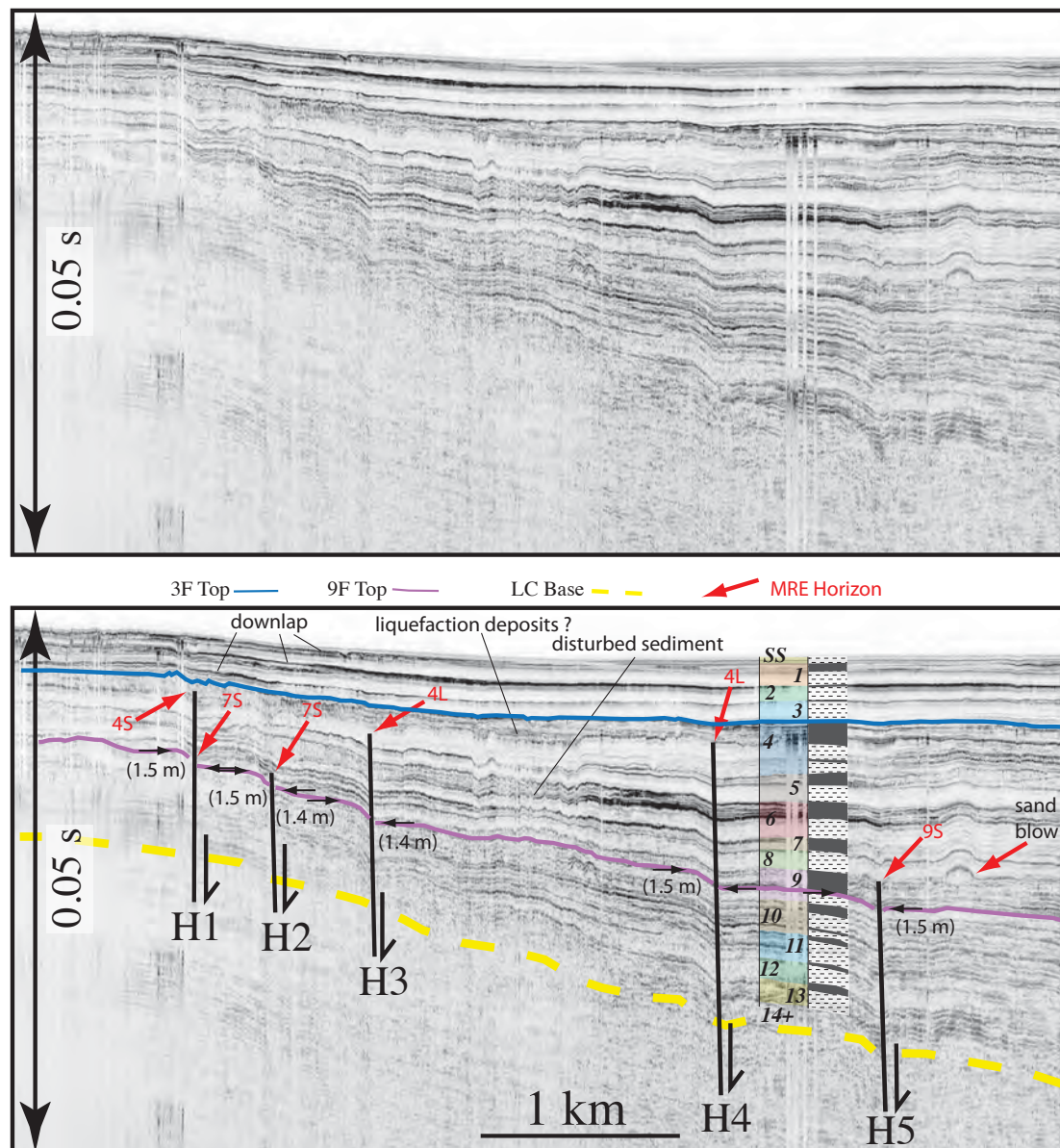


Figure 5-12: Type section across western hinge faults. Red arrows point to approximate event horizons. Due to the subtle nature of deformation, identifying event horizons is equivocal. Disturbed sediment and liquefaction dome (“sand blow”) may be seismically generated. Vertical folding over the base of 9S is consistently ~1.5 m for each fault.

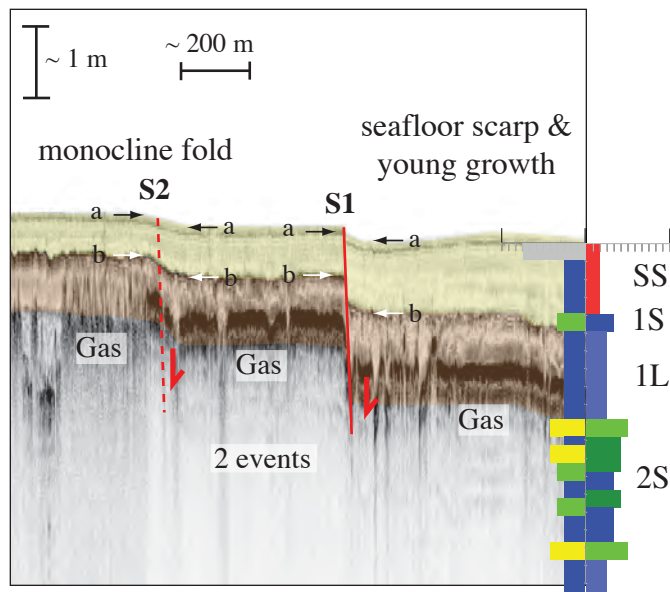


Figure 5-13: Most recent and penultimate offset along Faults S1 and S2. Distinctive seafloor scarps suggest displacement was recent, possibly coincident with the Elmore Ranch earthquake in 1987 (Hudnut et al., 1989b). However the relationship between onshore and offshore faults is not constrained. CPT soundings help define the stratigraphy obscured by acoustic wipeout zones (AWZs). Faults S1 and S2 may have experienced numerous earthquakes that are recorded in the deeper sediments below the AWZs.

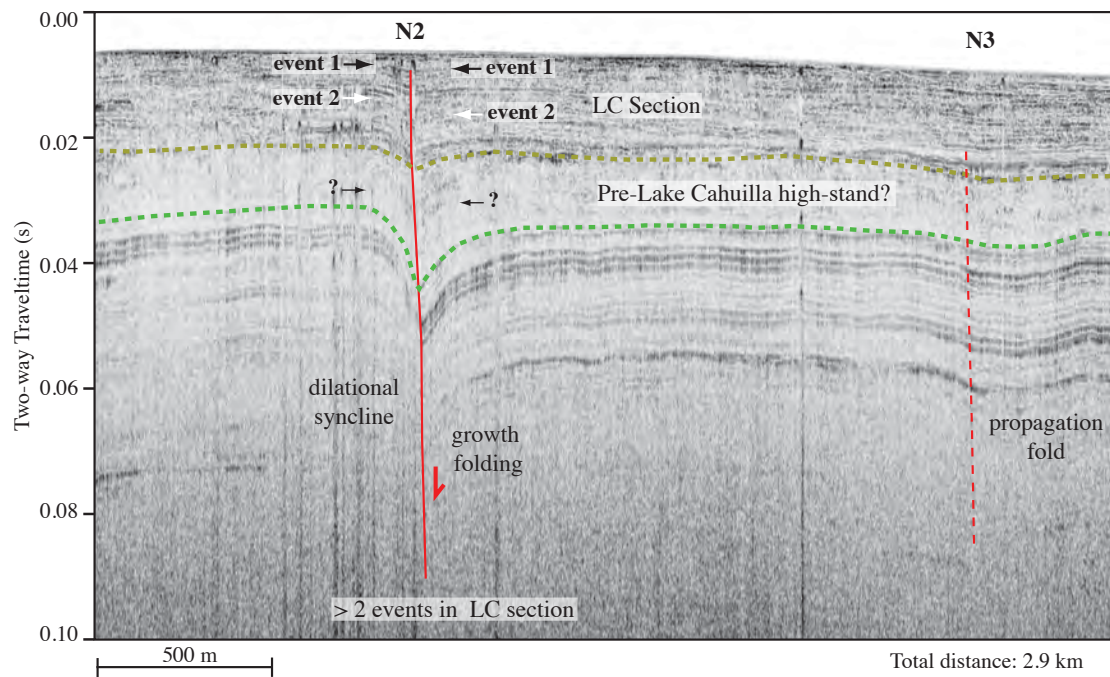


Figure 5-14: Northern faults N2 and N3. Growth folds have evidence for at least 2 events in the Lake Cahuilla section. Folding increases dramatically in the deeper section, which is inferred to be late Pleistocene in age. Based on the synclinal nature of deformation, fault N2 may accommodate a significant component of strike-slip motion.

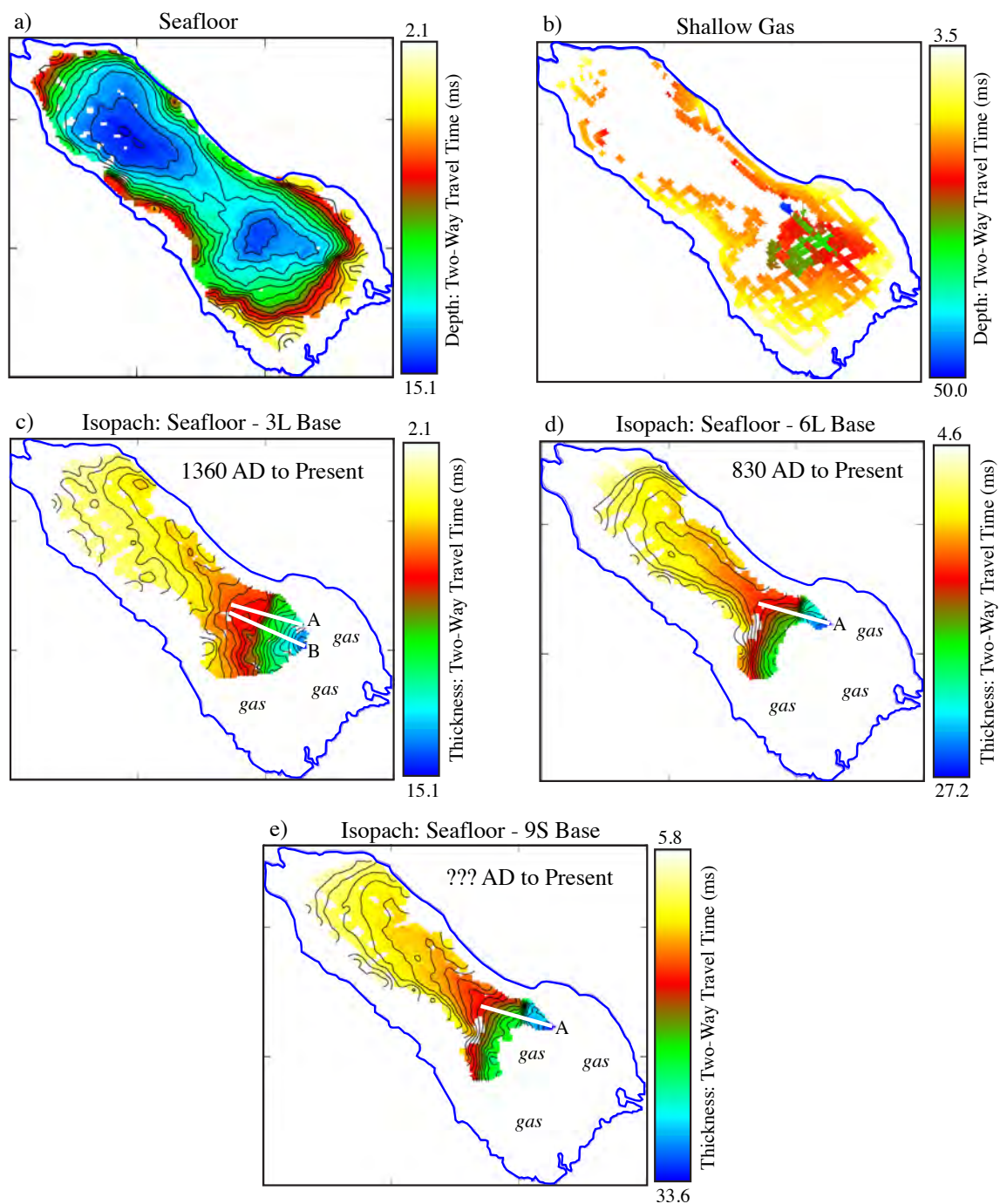


Figure 5-15: Contoured isopach calculations for 3 time horizons. Profiles A and B were used to calculate subsidence rates across the hinge zone. Rates are given in Table 3. We expect the subsidence measured here to be a minimum estimate. The inferred region of maximum subsidence to the south of the data coverage is closer to the sedimentation rate (~ 19 mm/yr), and based on the distinct topographic depression in the southern sea, we expect subsidence to outpace sedimentation.

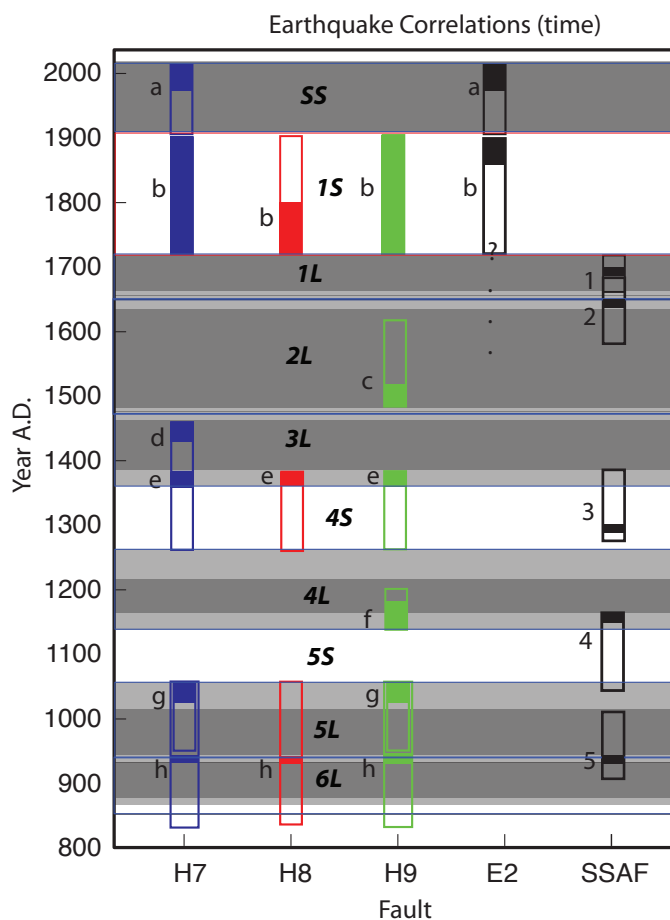


Figure 5-16: Comparison of earthquake chronologies between the Salton Sea and the Coachella site (following Philibosian, 2007). Filled rectangles are best estimates for timing, unfilled include the possible age range. Gray shades represent Lake Cahuilla high-stands. Dark shades are high-stands observed at 9m elevation (Philibosian, 2007) and light gray shades are times when shallow lakes persisted in the deeper portions of the basin. The best event correlation is between offshore event *h* and onshore event 5. Both appear to have occurred while lake 5 was flooding. Offshore event *f* and onshore event 4 are potential correlations. The rest of the events do not have unequivocal evidence for coincident timing. Events *e* and *c* occurred within the uncertainty bounds of onshore events 2 and 3. Despite close proximity of offshore faults and the SAF, the data do not show convincing evidence that these faults systems release strain in a synchronized manner. The most robust correlation is between offshore events and lake flooding (see Figure 9).

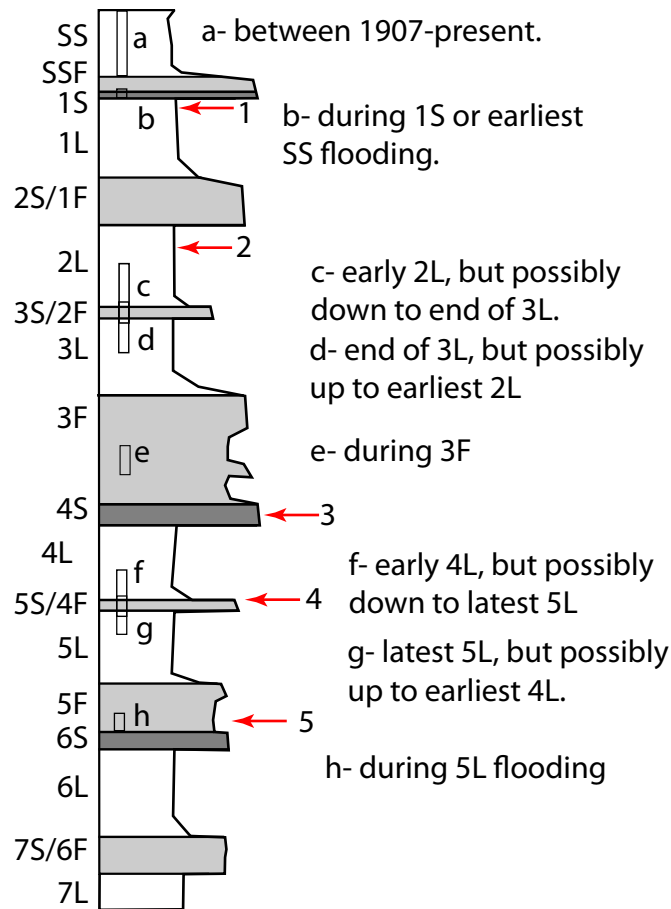


Figure 5-17: Relative stratigraphic positions between onshore (red arrows) and offshore (black rectangles) events. Event *b* occurred after a layer of subaerial coarse-grained material was deposited, suggesting it came several decades after event 1, which occurred when the high shoreline was still submerged in 1L. The lake would require ~60 years to desiccate before event *b* occurred. Events *c* and *d* appear to be distinct, taking place between the end of 3L and beginning of 2L, but their stratigraphic positions cannot be dissociated with complete certainty. Although event 2 occurred near the top of 2L and probably came after events *c* and *d*, the absolute timing differences cannot be resolved. Event *e* is seen during lake 3 flooding on faults H7, H8 and H9, but appears to have occurred after event 3, which is recorded in the mid-section of 4S. Events *f* and 4 correlate stratigraphically, as do events *h* and 5. It is important to note that events observed on one fault are often not observed on adjacent faults.